Politecnico di Torino

Master of Science in Physics of Complex Systems

Master Degree Thesis

Structural, Electronic and Magnetic Instabilities in Candidate Quantum Spin Liquid Honeycomb Iridates

Supervisor
Prof. A. Montorsi, Politecnico di Torino

Co-Supervisors
Dr. A. Subedi, École Polytechnique
Prof. G. C. Ghiringhelli, Politecnico di Milano

Candidate
Stefano Falletta

Academic Year 2017/2018

A mia mamma,
a mio papà
e a mio fratello

Summary

A special class of quantum paramagnets, known as quantum spin liquids (QSLs), have been attracting tremendous theoretical and experimental attention in the latest years. In this context, the goal of this thesis is to study the structural, electronic and magnetic properties of three candidate QSL materials, namely Na_2IrO_3, α-Li_2IrO_3 and $H_3LiIr_2O_6$, by performing DFT calculations with the inclusion of the Coulomb repulsion U and/or spin orbit coupling (SOC).

QSLs are systems in which spins are highly correlated and still fluctuate at $T = 0K$. This behaviour occurs in presence of large degeneracy in the system ground state, which can be due to frustration. Among the lattices in which QSL phases can arise, we consider honeycomb QSL, focusing specifically on the above mentioned iridates.

Despite the first candidate QSL honeycomb iridates Na_2IrO_3 and α-Li_2IrO_3 are experimentally found to order magnetically at low temperatures, the recently synthesized $H_3LiIr_2O_6$ does not show any magnetic ordering down to $1K$. To clarify the reasons why a QSL behaviour can be stabilized in $H_3LiIr_2O_6$, we perform ab initio DFT calculations for all the aforementioned materials, looking for the occurrence of instabilities that could inhibit the QSL state by lifting the degeneracy of the ground state.

The work is organized as follows. In chapter 1 we first introduce some general concepts on QSL and on their identification. In chapter 2, we focus specifically on honeycomb QSL, presenting some theoretical spin models (Kitaev model, Heisenberg-Kitaev model) and discussing the importance of

transition metal oxides, specifically of iridates, for the realization of the QSL behaviour. In chapter 3, we generate the theoretical structures for Na_2IrO_3, α-Li_2IrO_3 and $H_3LiIr_2O_3$ and then we perform ab initio DFT calculations with the inclusion of the Coulomb repulsion U and/or SOC, with the software QUANTUM ESPRESSO and VASP. Finally, in chapter 4 we review our results and propose next possible study directions.

Contents

List of Figures

List of Tables

Chapter 1

Introduction to Quantum Spin Liquids

It has long been recognized that in a spin system a paramagnetic ground state could be induced by strong quantum fluctuations, that are able to inhibit the long range magnetic ordering. A special class of quantum paramagnets is represented by the so-called quantum spin liquids (QSLs), that are attracting tremendous theoretical and experimental attention in the last years because of their extremely exotic properties and relationships to exotic forms of superconductivity [1]. Despite there is not an unique definition for a QSL system, common properties that characterize QSLs are:

- No spontaneous symmetry breaking at $T = 0K$, meaning that their ground state (GS) is disordered.
- Decaying long range spin correlations, i.e. $\langle \mathbf{S}_i \mathbf{S}_j \rangle \to 0$ as $|\mathbf{r}_i - \mathbf{r}_j| \to \infty$, being $\mathbf{S}_i$ the spin at position $\mathbf{r}_i$.
- Fractional excitations, which means that the excitations with respect to the ground state have fractional statistics.
- Long range quantum entanglement between the local degrees of freedom; this feature distinguishes QSL from other simpler paramagnets.

Typically these properties occur in presence of frustration, i.e. when the system cannot minimize its energy by minimizing the exchange energies between each group of interacting degrees of freedom. In spin models, frustration is induced by the geometry of the lattice and by the interactions between the degrees of freedom, which make the simultaneous minimisation of each term contributing to the energy impossible. This gives rise to a large degeneracy for the system ground state which, under certain conditions, leads to the QSL behaviour. The simplest example of frustration is represented by the anti-ferromagnetic Ising model on a triangular lattice, characterized by six possible ground states instead of the two ferromagnetic ground states (all spins up or down) for each triangle, as shown in Fig.1.1. Such degeneracy enhances fluctuations and suppresses order.

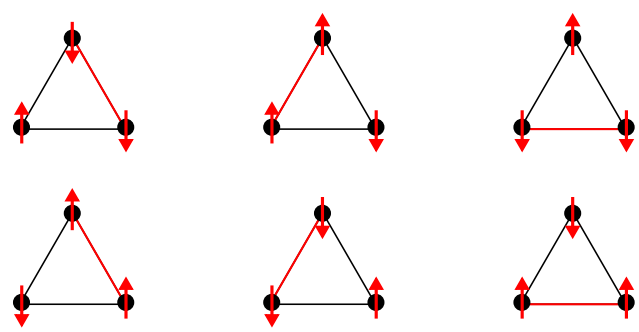

Figure 1.1: Ground state configurations for the anti-ferromagnetic Ising model on a triangle.

The strength of the frustration can be estimated by looking at the magnetic susceptibility at high temperatures. Indeed, for a local-moment magnet, the magnetic susceptibility χ recovers the Curie-Weiss form $\chi \approx C/(T - \Theta_{CW})$, being T the temperature, Θ_{CW} the Curie-Weiss temperature and C a constant. Large values of $|\Theta_{CW}|$ are associated to strong magnetic interactions and therefore to strong frustration. Then, a frustration parameter could be introduced as: $f = |\Theta_{CW}|/T_c$, being T_c the critical temperature below which orders freezes. For a spin liquid, we expect magnetic moments but no order and therefore f should go to infinity.

The research of QSLs is focused mostly on Mott insulators, that are systems characterized by localized electrons which still maintain their spin degree of freedom. For those systems it may happen that quantum fluctuations at $T = 0K$ make spins fluctuating without forming a magnetic ordering. The nature of those quantum fluctuations is different with respect to the one of classical fluctuations. Indeed, quantum fluctuations dominate for small values of spins (i.e. comparable with 1/2), whereas classical fluctuations dominate for large values of spins (i.e. much larger than 1/2) and are driven by the thermal energy, meaning that they cease at $T = 0K$.

There are many lattices where QSL phases can arise [2]; examples in 2D are the honeycomb lattice (Fig.1.2a), the Kagome lattice (Fig.1.2b), the Maple lead lattice (Fig.1.2c), the triangular lattice (Fig.1.2d); examples in 3D are the hyperkagome (Fig.1.2e) lattice and the pyrochlore lattice (Fig.1.2f).

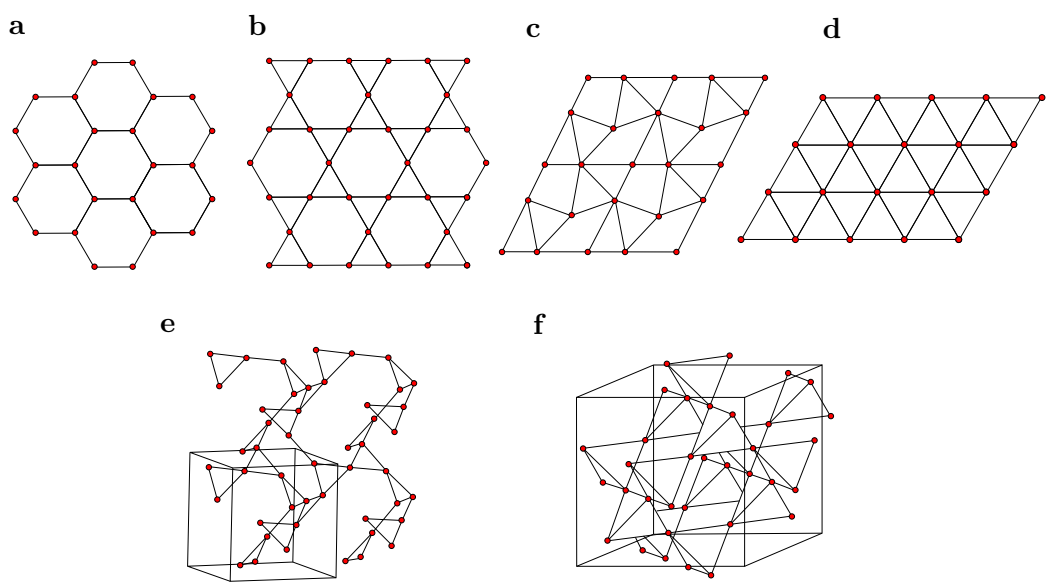

Figure 1.2: **a**, Honeycomb lattice. **b**, Kagome lattice. **c**, Maple leaf lattice. **d** Triangular lattice. **e** Hyperkagome lattice. **f** Pyrochlore lattice.

Nevertheless, the experimental identification of QSLs has proved to be very challenging. Indeed, there is no a single experimental signature that identifies uniquely a QSL state and therefore one should look at many features

of the material. Common experimental tools are [1]:

- Nuclear magnetic resonance to probe the presence of static moments.
- Specific heat measurements to get information on the low-energy density of states (DOS).
- Thermal transport to determine the nature of excitations (itinerant or localized).
- Elastic and inelastic neutron-scattering measurements to determine the nature of correlations and excitations.

There are a lot of candidate QSL materials that have been studied in the latest years; specifically, we focus on materials with a layered honeycomb structure. In the next chapter, we first present some theoretical spin models on a honeycomb lattice and then we introduce the materials we are interested in, that are the honeycomb iridates.

Chapter 2

Quantum Spin Liquids on a Honeycomb Lattice

2.1 Kitaev Model

In 2006, Kitaev proposed an exactly solvable model that offers a promising route to geometric frustration and, therefore, to a quantum spin liquid behaviour. It is a spin model on a honeycomb lattice with the following Hamiltonian:

$$H = -\sum_{\langle ij \rangle_{\gamma_{ij}}} K_{\gamma_{ij}} \sigma_i^{\gamma_{ij}} \sigma_j^{\gamma_{ij}} \qquad \gamma_{ij} = \begin{cases} x & \text{if } (i,j) \text{ is a } x \text{ link} \\ y & \text{if } (i,j) \text{ is a } y \text{ link} \\ z & \text{if } (i,j) \text{ is a } z \text{ link} \end{cases}$$

where:

- K_x, K_y and K_z are the Kitaev interactions; energy exchanges along neighbouring bonds cannot be satisfied simultaneously, giving rise to frustration and driving the system into the QSL phase.

- σ_j^x, σ_j^y, σ_j^z are the Pauli operators for the site j and they satisfy the

following relations:

$$[\sigma_j^\alpha \sigma_j^\beta] = 2i\epsilon_{\alpha\beta\gamma}\sigma_j^\gamma \qquad \{\sigma_j^\alpha, \sigma_j^\beta\} = 2\delta_{\alpha,\beta} I \qquad \sigma_j^\alpha \sigma_j^\beta = \delta_{\alpha,\beta} I + i\epsilon_{\alpha\beta\gamma}\sigma_j^\gamma$$

being $\epsilon_{\alpha,\beta,\gamma}$ the Levi-Civita symbol, $\delta_{\alpha,\beta}$ the Kronecker delta and I the identity matrix.

- $\langle i, j\rangle_{\gamma_{ij}}$ stands for nearest-neighbour sites i and j along a γ_{ij} bond.

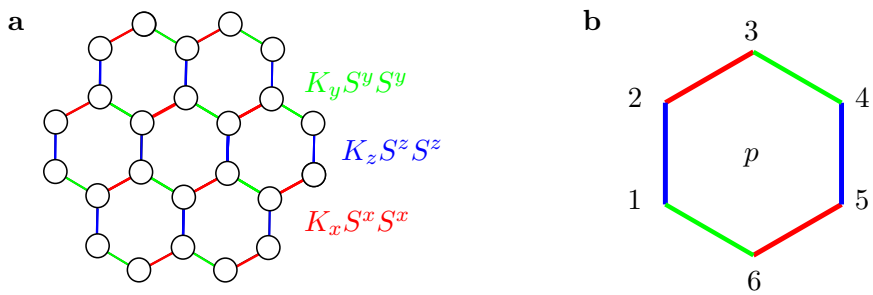

Figure 2.1: **a**, Hexagonal Lattice. **b**, Scheme of a plaquette p.

It is possible to map the spin operators into the Majorana operators b_j^x, b_j^y, b_j^z, c_j, which satisfy the following anti-commutation relations:

$$\{b_j^\alpha, b_j^\beta\} = \delta_{\alpha,\beta} \qquad \{b_j^\alpha, c_j\} = 1 \qquad \left(b_j^\alpha\right)^2 = 1 \qquad c_j^2 = 1$$

Let $\mathcal{M}$ be the physical 2-dimensional Hilbert space of a spin. In order to perform the fermionic mapping, we introduce an extended 4-dimensional Fock space $\tilde{\mathcal{M}}$ over which the Majorana operators act. Clearly $\mathcal{M} \subset \tilde{\mathcal{M}}$, therefore the Pauli operators σ_j^x, σ_j^y, σ_j^z acting on $\mathcal{M}$ can be represented by some operators $\tilde{\sigma}_j^x$, $\tilde{\sigma}_j^y$, $\tilde{\sigma}_j^z$ acting on $\tilde{\mathcal{M}}$. In particular, we choose:

$$\tilde{\sigma}_j^\alpha = i b_j^\alpha c_j \qquad \alpha = x, y, z$$

Upon the substitution $\sigma_j^\alpha \mapsto \tilde{\sigma}_j^\alpha = i b_j^\alpha c_j$, we have that $H \mapsto \tilde{H}$, which is given by:

$$\tilde{H} = -\sum_{\langle i,j\rangle_{\gamma_{ij}}} K_{\gamma_{ij}} \tilde{\sigma}_i^{\gamma_{ij}} \tilde{\sigma}_j^{\gamma_{i,j}} = -\sum_{\langle i,j\rangle_{\gamma_{ij}}} K_{\gamma_{ij}} \left(ib_i^{\gamma_{ij}} c_i\right)\left(ib_j^{\gamma_{ij}} c_j\right) =$$
$$= \frac{i}{2} \sum_{\langle i,j\rangle_{\gamma_{ij}}} 2K_{\gamma_{ij}} \left(ib_i^{\gamma_{ij}} b_j^{\gamma_{ij}}\right) c_i c_j$$

By introducing the operator $\hat{u}_{ij} = ib_i^{\gamma_{ij}} b_j^{\gamma_{ij}}$, we obtain:

$$\tilde{H} = \frac{i}{4} \sum_{i,j} \tilde{A}_{ij} c_i c_j \qquad \tilde{A}_{jk} = \begin{cases} 2K_{\gamma_{ij}} \hat{u}_{jk} & \text{if } i \text{ and } j \text{ are connected} \\ 0 & \text{otherwise} \end{cases}$$

We notice that $\tilde{H}$ is quadratic, meaning that our system is described by free Majorana fermions.

We now introduce the plaquette operator W_p for the plaquette p:

$$W_p = \sigma_1^x \sigma_2^y \sigma_3^z \sigma_4^x \sigma_5^y \sigma_6^z = \prod_{\langle i,j\rangle_{\gamma_{ij}} \in p} \sigma_i^{\gamma_{ij}} \sigma_j^{\gamma_{ij}}$$

We notice that $[W_p, H] = 0$ and $[W_p, W_{p'}] = 0$ for $p \neq p'$, therefore W_p is an integral of motion. Moreover, W_p has eigenvalues $\omega_p = \pm 1$. Upon the substitution $\sigma_j^\alpha \mapsto \tilde{\sigma}_j^\alpha = ib_j^\alpha c_j$, we have that $W \mapsto \tilde{W}$, which is given by:

$$\tilde{W}_p = \prod_{\langle i,j\rangle_{\gamma_{ij}} \in p} \tilde{\sigma}_i^{\gamma_{ij}} \tilde{\sigma}_j^{\gamma_{ij}} = \prod_{\langle i,j\rangle_{\gamma_{ij}} \in p} \hat{u}_{ij}$$
$$\omega_p = \prod_{\langle i,j\rangle_{\gamma_{ij}} \in p} u_{ij}$$

The variables u_{kj} can be interpreted as a $\mathcal{Z}_2$ gauge field, whereas ω_p can be thought as the magnetic flux through the plaquette p. We denote by vortex-free configuration the one such that $\omega_p = 1\ \forall p$. Whereas if $\omega_p = -1$, we say that the plaquette carries a vortex.

It turns out that the ground state configuration occurs in the vortex-free field configuration. Therefore, it can be achieved for example in the case $u_{ij} =$

1 $\forall(i,j)$. We notice that this field configuration possesses a translational symmetry, therefore we can switch to the Fourier space to analytically find the spectrum. First, let us introduce a new notation; we refer to the site index j by specifying:

- s: label unit cell
- λ: position inside the unit cell

By switching $j \to (s,\lambda)$ the Hamiltonian becomes:

$$\tilde{H} = \frac{i}{4} \sum_{s,\lambda,t,\mu} \tilde{A}_{s\lambda,t\mu} c_{s\lambda} c_{t\mu}$$

It is possible to prove that the coefficients $A_{s\lambda,t\mu}$ actually depend only on λ, μ and $t-s$. Then, we Fourier expand $A_{s\lambda,t\mu}$ and $c_{s\lambda}$ as:

$$\begin{cases} A_{s\lambda,t\mu} = \frac{1}{N} \sum_{\mathbf{q}} e^{-i\mathbf{q}(\mathbf{r}_t - \mathbf{r}_s)} \tilde{A}_{\lambda\mu}(\mathbf{q}) \\ c_{s\lambda} = \frac{1}{\sqrt{N}} \sum_{\mathbf{q}} e^{i\mathbf{q}\mathbf{r}_s} a_{\mathbf{q}\lambda} \end{cases}$$

where N is the total number of unit cells. Therefore, the Hamiltonian can be rewritten as:

$$\tilde{H} = \frac{i}{4} \sum_{s,\lambda,t,\mu} \left(\frac{1}{N} \sum_{\mathbf{q}} e^{-i\mathbf{q}(\mathbf{r}_t - \mathbf{r}_s)} \tilde{A}_{\lambda\mu}(\mathbf{q}) \right) \left(\frac{1}{\sqrt{N}} \sum_{\mathbf{q}'} e^{i\mathbf{q}'\mathbf{r}_s} a_{\mathbf{q}'\lambda} \right) \left(\frac{1}{\sqrt{N}} \sum_{\mathbf{q}''} e^{i\mathbf{q}''\mathbf{r}_t} a_{\mathbf{q}''\mu} \right) =$$
$$= \frac{i}{4} \sum_{\mathbf{q},\mathbf{q}',\mathbf{q}'',\lambda,\mu} \tilde{A}_{\lambda\mu}(\mathbf{q}) a_{\mathbf{q}'\lambda} a_{\mathbf{q}''\mu} \delta_{\mathbf{q},-\mathbf{q}'} \delta_{\mathbf{q},\mathbf{q}''} = \frac{i}{4} \sum_{\mathbf{q},\lambda,\mu} \tilde{A}_{\lambda\mu}(\mathbf{q}) a_{-\mathbf{q}\lambda} a_{\mathbf{q}\mu}$$

We choose a basis $(\mathbf{n}_1, \mathbf{n}_2)$ of the translation group, with $\mathbf{n}_1 = \left(\frac{1}{2}, \frac{\sqrt{3}}{2}\right)$ and $\mathbf{n}_2 = \left(-\frac{1}{2}, \frac{\sqrt{3}}{2}\right)$. Then, we obtain that $\tilde{A}_{\lambda\mu}(\mathbf{q})$ is given by:

$$\tilde{A}_{\lambda\mu}(\mathbf{q}) = \sum_t e^{i\mathbf{q}\mathbf{r}_t} A_{0\lambda,t\mu} = \begin{pmatrix} 0 & f(\mathbf{q}) \\ f^*(\mathbf{q}) & 0 \end{pmatrix}$$

$$f(\mathbf{q}) = 2\left(K_x e^{i\mathbf{q}\mathbf{n}_1} + K_y e^{i\mathbf{q}\mathbf{n}_2} + K_z\right)$$

and the spectrum is given by:

$$\epsilon(\mathbf{q}) = \pm|f(\mathbf{q})|$$

We notice that the spectrum can be gapless if $f(\mathbf{q}) = 0$. This equation has solutions if and only if $|K_x|$, $|K_y|$, $|K_z|$ satisfy the triangle inequalities:

$$|J_x| \leq |J_y| + |J_z| \qquad |J_y| \leq |J_x| + |J_z| \qquad |J_z| \leq |J_x| + |J_y|$$

For strict inequalities ($<$) there are two solutions: $\mathbf{q} = \pm\mathbf{q}^*$. At those points, the spectrum has conic singularities with a Dirac cone like dispersion relation. Fractional excitations are generated in both cases of gapped or gapless spectrum [3].

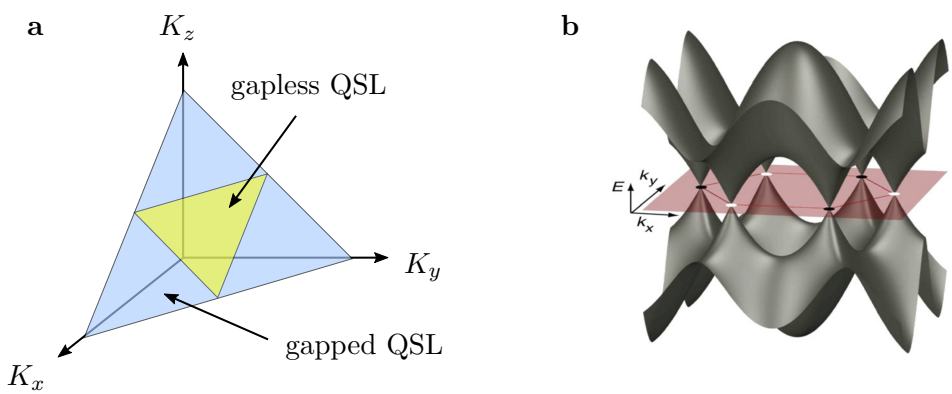

Figure 2.2: **a**, Phase diagram of the Kitaev model [4]. **b**, Dirac dispersion relation in the gapless QSL phase.

2.2 Heisenberg-Kitaev Model

The Kitaev model can be improved by including other kind of interactions in the Hamiltonian. By inserting the Heisenberg interactions and considering isotropic Kitaev exchanges, we get the Heisenberg-Kitaev Hamiltonian:

$$H = -\sum_{\langle i,j\rangle_{\gamma_{ij}}} \left[2K S_i^{\gamma_{ij}} S_j^{\gamma_{ij}} + J\mathbf{S}_i\mathbf{S}_j\right] \qquad \gamma_{ij} = \begin{cases} x & \text{if } (i,j) \text{ is a } x \text{ link} \\ y & \text{if } (i,j) \text{ is a } y \text{ link} \\ z & \text{if } (i,j) \text{ is a } z \text{ link} \end{cases}$$

Let us introduce the energy scale $A = \sqrt{K^2 + J^2}$ and the angle ϕ such that $K = A\sin\phi$ and $J = A\cos\phi$. Then, the Hamiltonian can be rewritten as:

$$H = -\sum_{\langle i,j\rangle_{\gamma_{ij}}} A\left[2\sin\phi\ S_i^{\gamma_{ij}} S_j^{\gamma_{ij}} + \cos\phi\ \mathbf{S}_i\mathbf{S}_j\right]$$

As ϕ varies from 0 to 2π, we get many phases for the ground state: the QSL phase, the ferromagnetic phase and the anti-ferromagnetic Néel, stripy, zigzag phases, as shown in Fig.2.3; black/white circles refer respectively to up/down spins or vice versa. Further refinements of this model could be done in principle by introducing next neighbours interactions [5].

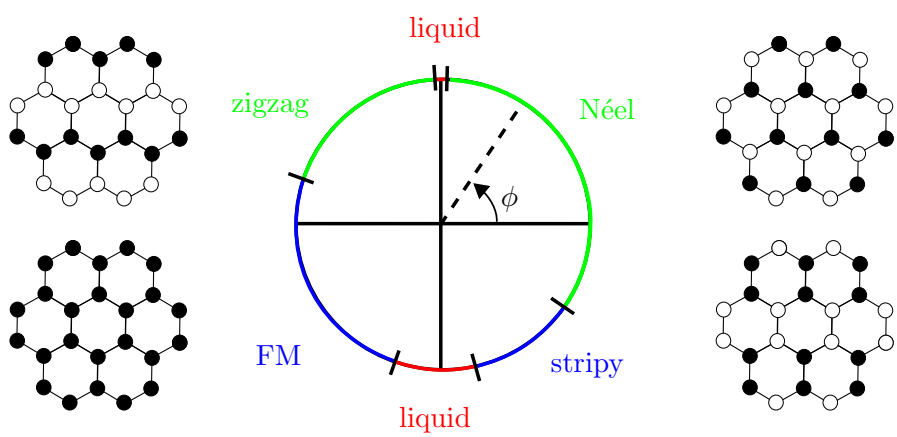

Figure 2.3: Phase diagram diagram of the Heisenberg-Kitaev model [6].

2.3 Transition Metal Oxides

Finding materials in which the QSL ground state is realized is very challenging. In this perspective, transition metal oxides (TMO) are quite interesting because they display an unique interplay of:

- Crystal Field CF
- Spin orbit coupling SOC
- Coulomb repulsion U

Moving down in the periodic table, from $3d$ to $4d$ to $5d$ transition metals, the on-site Coulomb repulsion decreases ($U_{3d} > U_{4d} > U_{5d}$), since the d orbitals become more extended. On the other hand, the spin orbit coupling increases ($SOC_{3d} < SOC_{4d} < SOC_{5d}$) because the atomic number Z increases (SOC grows with $\sim Z^2$ by considering also screening effects [7]). In iridates, the energy scales of CF, U and SOC are all comparable and thus compete with each other, giving rise to interesting effects.

Electron Type	$U[eV]$	$SOC[eV]$	Spin State	Interactions
$3d$	5-7	0.01-0.1	High	$U_{3d} > CF_{3d} > SOC_{3d}$
$4d$	0.5-0.3	0.1-0.3	Low/Intermediate	$U_{4d} \sim CF_{4d} > SOC_{4d}$
$5d$	0.4-2	0.1-1	Low	$U_{5d} \sim CF_{5d} \sim SOC_{5d}$

Table 2.1: Comparison of CF, U and SOC in $3d$, $4d$ and $5d$ materials [7].

In particular, we consider iridates that have in their structure IrO_6 octahedra, in which an Ir atom is surrounded by six O^{2-} atoms. This configuration gives rise to a crystal field which hinders the free motion of d-electrons. Indeed, the octahedral crystal field splits the 5-fold degenerate d-levels (d_{xy}, d_{yz}, d_{xz}, $d_{x^2-y^2}$, d_{z^2}) into 2-fold degenerate e_g levels ($d_{x^2-y^2}$, d_{z^2}) with higher energy and 3-fold degenerate t_{2g} levels (d_{xy}, d_{yz}, d_{xz}) with lower energy. Then, the SOC splits the t_{2g} levels into d_{xy} level with higher energy and degenerate d_{xz} and d_{yz} levels with lower energy. The actual filling arrangement depends

on the competition between energy spacings and on-site exchange interaction described by Hund's rule. In IrO_6 octahedra, Ir^{4+} have 5 electrons in the d-orbitals and they arrange such that there is only one unpaired electron in the d_{xy} orbital (Fig.2.4). This gives rise to a system with an effective angular momentum $J_{eff} = \frac{1}{2}$, which represents indeed a spin-orbital Mott state sitting on the Ir^{4+} atom.

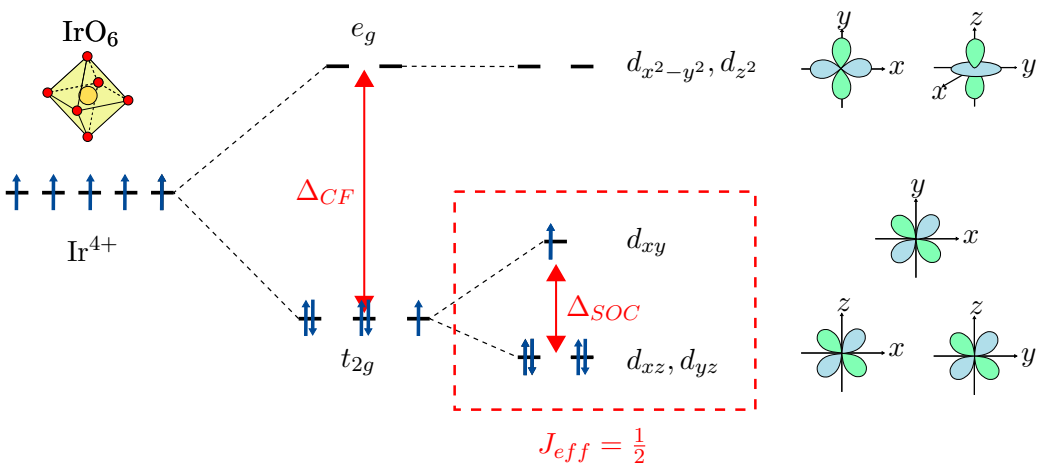

Figure 2.4: Splitting energy levels in IrO_6 due to the octahedral crystal field and to *SOC* [8].

2.4 Honeycomb Iridates

Examples of spin-orbital Mott insulators are the sodium iridate Na_2IrO_3 and the lithium iridate α-Li_2IrO_3. $NaIrO_3$ (α-Li_2IrO_3) crystallizes in a layered structure in which IrO_6 octahedra form a honeycomb network by sharing three orthogonal edges to other IrO_6 octahedra and other three orthogonal edges to NaO_6 (LiO_6) octahedra; the interlayer spacing is filled with Na (Li) atoms. The experimental lattice parameters and atomic coordinates of these two materials are reported in Tab.2.2.

In both Na_2IrO_3 and α-Li_2IrO_3 we have that:

- The magnetic susceptibility recovers a Curie-Weiss behaviour over a

Na_2IrO_3 - Space Group $C2/m$			
Atom	x	y	z
Ir	0.5000	0.1671	0.0000
Na	0.0000	0.0000	0.0000
Na	0.5000	0.0000	0.5000
Na	0.5000	0.3402	0.5000
O	0.7486	0.1782	0.7896
O	0.7117	0.0000	0.2047
$a = 5.4271$Å, $b = 9.3951$Å, $c = 5.6141$Å			
$\alpha = 90°$, $\beta = 109.037°$, $\gamma = 90°$			

α-Li_2IrO_3 - Space Group $C2/m$			
Atom	x	y	z
Ir	0.0000	0.3332	0.0000
Li	0.0000	0.0000	0.0000
Li	0.0000	0.8096	0.5000
Li	0.0000	0.5000	0.5000
O	0.2524	0.3161	0.7592
O	0.2565	0.0000	0.7883
$a = 5.1633$Å, $b = 8.9294$Å, $c = 5.1219$Å			
$\alpha = 90°$, $\beta = 109.759°$, $\gamma = 90°$			

Table 2.2: Experimental structural parameters of Na_2IrO_3 [9] and of α-Li_2IrO_3 [10].

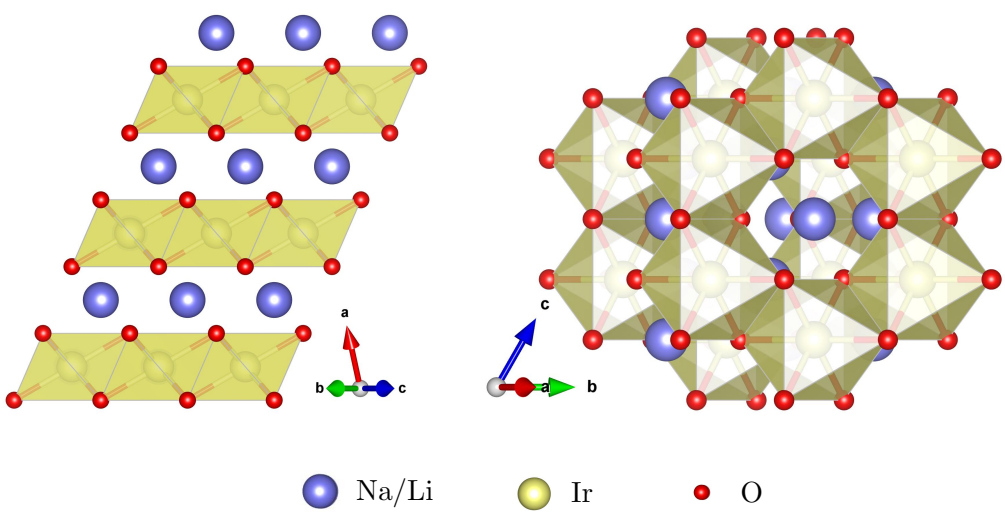

Figure 2.5: Experimental C2/m crystal structure of Na_2IrO_3 and α-Li_2IrO_3.

certain temperature, that confirms the presence of localized magnetic moments (Fig.2.6a).

- The specific heat shows a peak in correspondence of a certain temperature, called Néel temperature, around $15K$ (Fig.2.6b), meaning that a phase transition towards a magnetic order occurs.

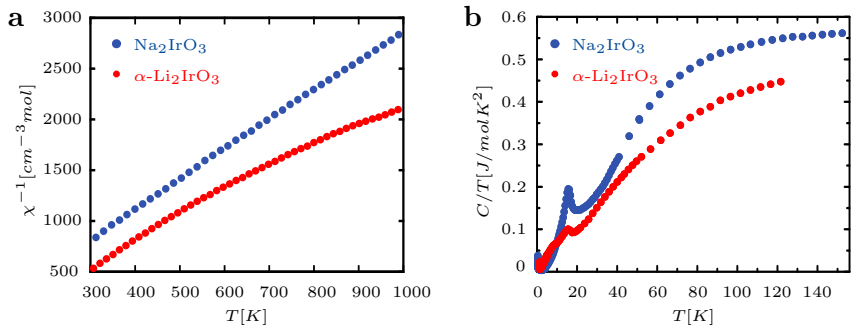

Figure 2.6: **a**, Experimental data of the inverse susceptibility in Na_2IrO_3 and α-Li_2IrO_3 [11]. **b**, Experimental data of the heat capacity in Na_2IrO_3 and α-Li_2IrO_3 [11].

Indeed experimentally Na_2IrO_3 shows an anti-ferromagnetic zigzag ordering (Fig.2.7a), whereas α-Li_2IrO_3 shows an incommensurate spiral structure i.e. counter-rotating spirals on zigzag chains (Fig.2.7b).

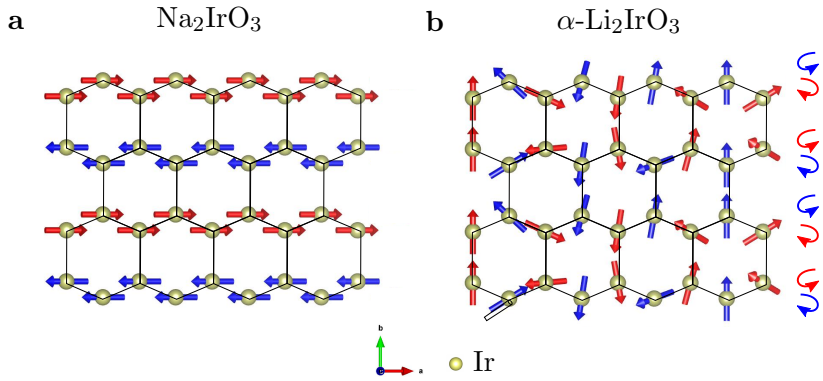

Figure 2.7: **a**, Experimental GS of Na_2IrO_3. **b**, Experimental GS of α-Li_2IrO_3.

The difficulty in realizing a QSL behavior in the aforementioned materials motivates us to explore other honeycomb-based Ir^{4+} oxides. In particular,

we consider $H_3LiIr_2O_6$, that can be obtained from α-Li_2IrO_3 by replacing the interlayer Li^+ ions with H^+ ions [10].

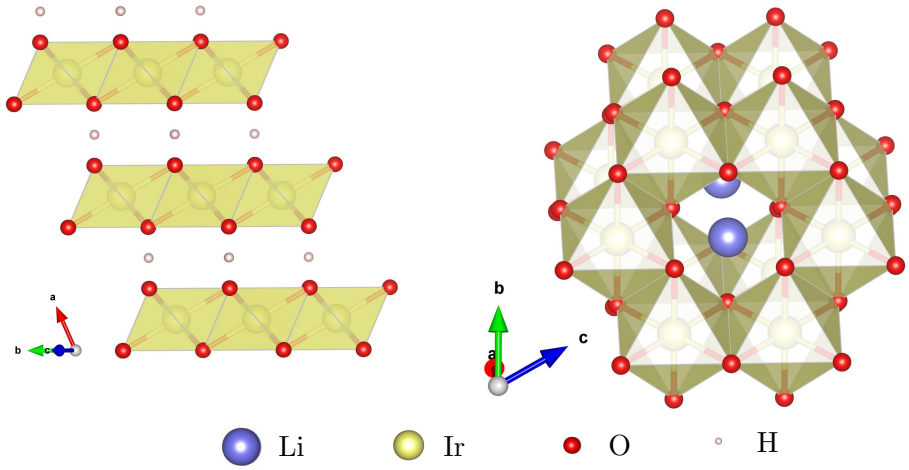

Figure 2.8: Experimental C2/m crystal structure of $H_3LiIr_2O_6$.

A Curie-Weiss behaviour is observed in the inverse magnetic susceptibility (Fig.2.9a) and no trace of phase transition is observed in the specific heat (Fig.2.9b), in sharp contrast to the other Kitaev candidates.

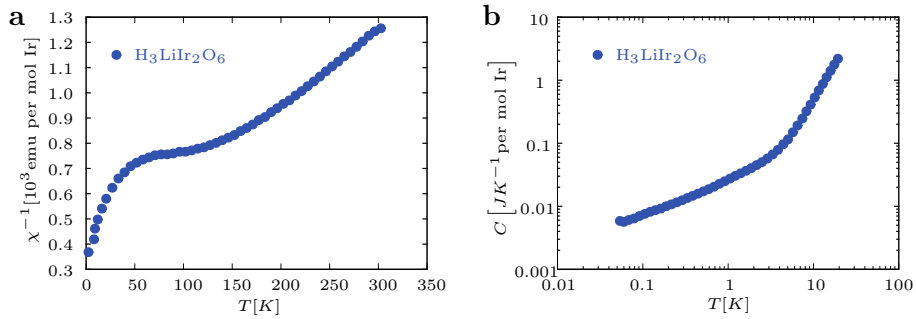

Figure 2.9: **a**, Experimental data of the inverse susceptibility in $H_3LiIr_2O_6$ [12]. **b**, Experimental data of the heat capacity in $H_3LiIr_2O_6$ [12].

These results suggest that the ground state of $H_3LiIr_2O_6$ is a liquid state of $J_{eff} = 1/2$ moments. To clarify the reason why a QSL behaviour can

be stabilized in $H_3LiIr_2O_6$, a detailed structural understanding of all the aforementioned iridates is necessary.

Chapter 3

First-Principle Calculations on Honeycomb Iridates

We perform first-principles calculations to investigate the structural stability and the electronic and magnetic properties of Na_2IrO_3, α-Li_2IrO_3 and $H_3LiIr_2O_6$. The calculations are performed within the framework of Density Functional Theory (DFT) and implemented with two software: Quantum ESPRESSO (QE) [13] and VASP [14–17]. This allows to compare the results obtained in two different ways and therefore to better assess their validity.

In QE we treat ions and core electrons with ultrasoft pseudopotentials: in absence of SOC we use non relativistic GBRV pseudopotentials, whereas in presence of SOC we use fully relativistic PseudoDojo pseudopotentials. Instead, in VASP we use Projected Augmented Wave (PAW) potentials. For the exchange-correlation part of electron-electron interactions we adopt the generalized gradient approximations (GGA) formalism as described by Perdew-Burke-Ernzerhof (PBE). In order to model the strong correlations, we use the GGA+U approach, following the simplified version of DFT+U calculation proposed by Cococcioni and De Gironcoli [18]. Relevant DFT parameters are:

- E_{cut}: energy cut-off for the plane wave expansion.

- $E_{cut,charge}$: energy cut-off for the charge density.
- $\mathbf{k}_{grid}$: Monkhorst-Pack grid for the self consistent calculation.
- $\mathbf{k}_{grid}^{nscf}$: Monkhorst-Pack grid for the non self consistent calculation.
- n_k: number of k points along a path between two high symmetry points.
- β_{mix}: mixing factor.
- δ_{gauss}: Marzari-Vanderbilt smearing.

Convergences tests reveal that a good set of values for the above mentioned parameters in QE and VASP is the one shown in Tab.3.1; further details are reported in Appendix A. Finally, in QE we use local-density-dependent Thomas Fermi screening to help calculations converge.

Parameters	QE	VASP
E_{cut}	80 Ry	600 eV
$E_{cut,rho}$	680 Ry	-
$\mathbf{k}_{grid}$	(12,12,12)	(8,8,8)
$\mathbf{k}_{grid}^{nscf}$	(16,16,16)	-
n_k	300	-
β_{mix}	0.01	0.01
δ_{gauss}	10^{-6}	10^{-6}

Table 3.1: Parameters used for DFT calculations in QE and VASP for a primitive cell.

We first generate all the possible structures for Na_2IrO_3, α-Li_2IrO_3 and $H_3LiIr_2O_6$, according to the different allowed stackings of their layers. After, we perform a non magnetic relax DFT calculation, in order to determine the lowest energy structure for each material. Then, we carry further studies introducing magnetism, U and SOC step-by-step. We are interested in studying the occurrence of instabilities, that are mechanisms that break the degeneracy of the ground state. We are interested in four kind of instabilities:

- Structural instability, due to distortions of the lattice structure from the ideal one (perfect Ir-honeycomb lattice in the case of Na_2IrO_3, α-Li_2IrO_6 and $H_3LiIr_2O_6$).
- Electronic instability, that can be identified by looking at the electronic bands and density of states (DOS).
- Magnetic instability, that occurs when a magnetic configuration has lower energy than the non magnetic configuration.
- Phonon instability, that arises when the phononic dispersion relation contains imaginary frequencies.

3.1 Generation Initial Structures

First, we generate the atomic positions for Na_2IrO_3, α-Li_2IrO_3 and $H_3LiIr_2O_6$ for all the possible allowed theoretical structures. To do that, we:

1. Reproduce the honeycomb layers of IrO_6 octahedra.
2. Stack the layers according to all the possible allowed stackings.
3. Put interlayer atoms according to all the possible positions.

In order to generate honeycomb layers, we first consider hexagonal layers of edge sharing IrO_6 octahedra. In this case there are only three possible positions that can be assumed by the atoms, that we label as A, B, C. Considering a primitive cell, the fractional coordinates of these positions are:

$$A = \left(\frac{1}{3}, \frac{2}{3}, \xi\right) \qquad B = (0, 0, \xi) \qquad C = \left(\frac{2}{3}, \frac{1}{3}, \xi\right)$$

where ξ controls the stacking sequence. It is possible to switch from hexagonal to honeycomb symmetry just by replacing the diagonal Ir atoms with Na/Li atoms, as shown in Fig.3.1. Then, there are only 4 possibilities to stack those honeycomb layers, that are labelled as O3, P3, T1 and P2 [19].

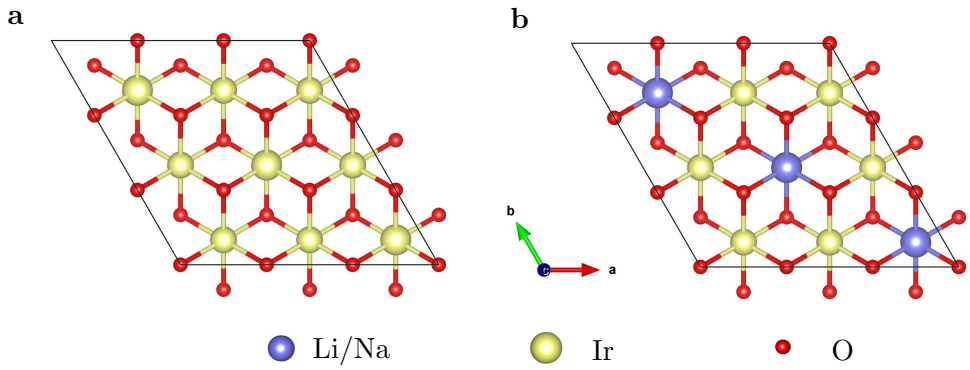

Figure 3.1: **a**, Hexagonal network of Ir atoms. **b**, Honeycomb network of Ir atoms.

As it is shown in Fig.3.2, these stackings basically differ for the sequence of positions that are assumed by the atoms.

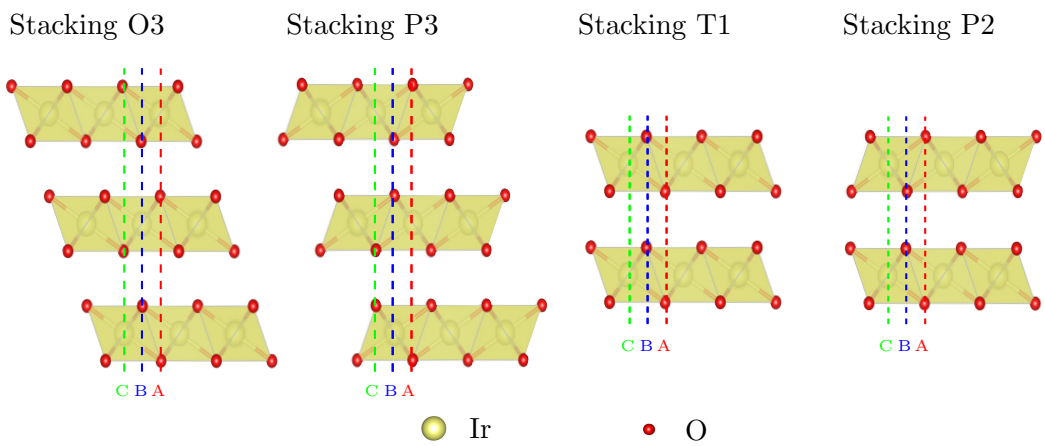

Figure 3.2: Stacking patterns for layers (interlayer atoms are missing).

Finally, interlayer atoms can assume the positions A, B, C. Therefore, moving from down layers up to top layers, the atomic positions must follow one of these possible sequences:

- O3-$\alpha\beta\gamma = ACB$-α-CBA-β-BAC-γ
- P3-$\alpha\beta\gamma = ACB$-α-BAC-β-CBA-γ
- T1-$\alpha\beta = ACB$-α-ACB-β

- P2-$\alpha\beta = ACB$-α-BCA-β

We generate the atomic positions for all these stackings using the Pymatgen library in Python. With the perspective to perform relaxation calculations later, we set the values of lattice parameters of the primitive cell as indicated in Tab.3.2. Then, for stackings O3 and P3 we consider a supercell 3x3x3 of the primitive cell, whereas for stackings T1 and P2 we consider a supercell 3x3x2 of the primitive cell. The atomic coordinates and cell parameters for the various stacked structures are reported in Appendix B.

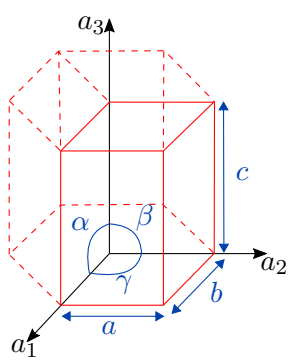

Figure 3.3: Hexagonal crystal structure.

Lattice Parameters	
a	3.5Å
b	3.5Å
c	4.7Å
α	90°
β	90°
γ	120°

Table 3.2: Initial lattice parameters for the hexagonal cell to relax.

Clearly, the species of the intralayer and interlayer atoms discriminate the cases of α-Li_2IrO_3, Na_2IrO_3 and $H_3LiIr_2O_6$. It is also very useful to check the correctness of the structures using VESTA [20], a software that allows to visualize the 3D structure of a material and measure the atomic distances and angles between atoms.

3.2 Non Magnetic Relax DFT Calculations

Given the whole set of lattice structures for Na_2IrO_3, α-Li_2IrO_3 and $H_3LiIr_2O_6$, we now want to determine the lowest energy structure for each of these materials. Since we are only interested in the structure, at this stage we perform

non magnetic calculations, i.e. we do not initialize any magnetic moment on Ir atoms. For each initial theoretical structure, we carry out a variable-cell relax calculation, which changes the lattice and moves the atoms to reduce respectively the stress and the forces. Both ion and cell dynamics are solved according to the BFGS quasi-newton algorithm, which is an iterative method for solving unconstrained nonlinear optimization problems. Then, we compare the electronic ground state energy for all the possible stackings of the layers for α-Li_2IrO_3 and $H_3LiIr_2O_6$.

It turns out that:

- The lowest energy stacking for α-Li_2IrO_3 is O3-ACB both in QE (Fig.3.4.a) and in VASP (Fig.3.5.a), which is in agreement with the experimental observations.

- The lowest energy stackings for $H_3LiIr_2O_6$ are P3-CBA, P2-AB, P2-BA in QE (Fig.3.4.b) and P3-CBA, P2-AB in VASP (Fig.3.5.b). Since this material is obtained starting from α-Li_2IrO_3 and replacing the interlayer Li atoms with H atoms, it makes more sense to focus on the P3-CBA stacking, which is also the experimental stacking.

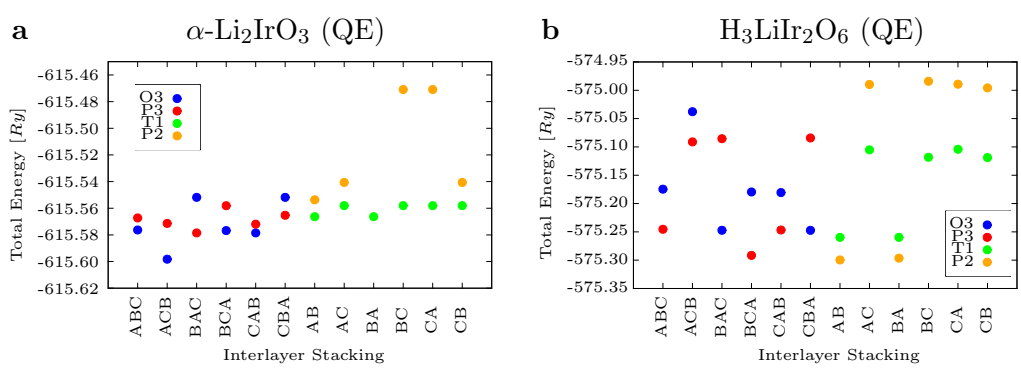

Figure 3.4: **a**, GS energies (QE) of all the possible stacking structures for non magnetic α-Li_2IrO_3. **b**, GS energies (QE) of all the possible stacking structures for non magnetic $H_3LiIr_2O_6$.

Thus, the lowest energy stacking for $H_3LiIr_2O_6$ differs with respect to the stacking for α-Li_2IrO_3. This is due to the fact that H^+ ions are less space

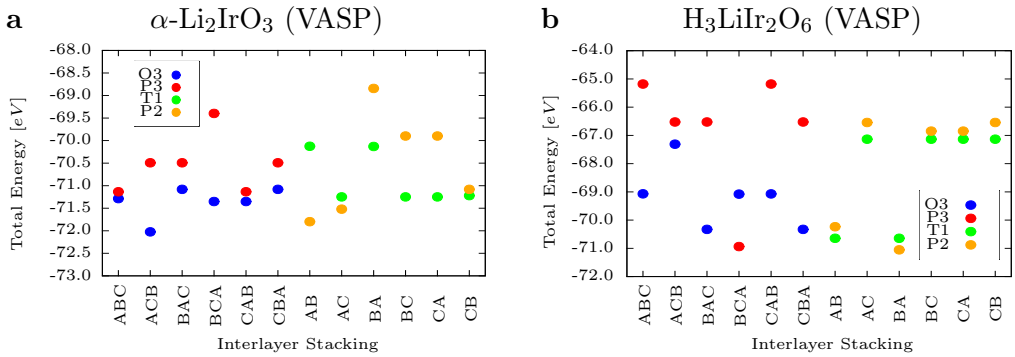

Figure 3.5: **a**, GS energies (VASP) of all the possible stacking structures for non magnetic α-Li_2IrO_3. **b**, GS energies (VASP) of all the possible stacking structures for non magnetic $H_3LiIr_2O_6$.

filling than Li^+ ions, then the interlayer distance decreases and H atoms tend to form 180° with O atoms. From now on, we will consider only one stacking per material, that is the O3-ACB for Na_2IrO_3 and α-Li_2IrO_3 and the P3-BCA for $H_3LiIr_2O_6$. The theoretical atomic distances Ir-O and Li-O in the relaxed structures of α-Li_2IrO_3 (stacking O3-ACB) and $H_3LiIr_2O_6$ (stacking P3-BCA) are reported in Tab.3.3. We introduce an enumeration for the bonds, that is shown in Fig.3.6.

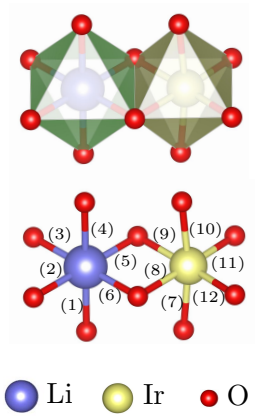

Figure 3.6: In-plane LiO_6 and IrO_6 octahedra in the crystal structures of α-Li_2IrO_3 and $H_3LiIr_2O_6$.

Atomic Distances [Å]				
	QE		VASP	
Bond	α-Li_2IrO_3	$H_3LiIr_2O_6$	α-Li_2IrO_3	$H_3LiIr_2O_6$
Li-O (1)	2.19346	2.15273	2.38213	2.13797
Li-O (2)	2.03949	2.16964	2.28268	2.16996
Li-O (3)	2.03949	2.16964	1.92643	2.16996
Li-O (4)	2.19356	2.15273	2.01887	2.13797
Li-O (5)	2.03949	2.16964	1.92643	2.16996
Li-O (6)	2.03949	2.16964	2.28268	2.16996
Ir-O (7)	2.08040	2.02374	2.13736	2.02430
Ir-O (8)	2.01240	2.02218	2.10879	2.02190
Ir-O (9)	2.01240	2.02218	1.99501	2.02190
Ir-O (10)	2.08040	2.02374	2.02914	2.02430
Ir-O (11)	2.04553	2.02520	2.03646	2.02972
Ir-O (12)	2.04553	2.02520	2.08676	2.02972

Table 3.3: Atomic distances of the relaxed crystal structures in α-Li_2IrO_3 (stacking O3-ACB) and $H_3LiIr_2O_6$ (stacking P3-BCA) computed with VESTA.

In QE, the relaxed structures of α-Li_2IrO_3 and $H_3LiIr_2O_6$ are characterized by equal Li-O (2) (3) (5) (6) distances, which is expected because of the symmetry of the lattice. On the other hand, the IrO_6 octahedra show shorter Ir-O (8) (9) distances with respect to Ir-O (11) (12); this distortion is due to the fact that oxygen atoms involved in bonds (8) (9) are in between Li and Ir, whereas oxygen atoms involved in bonds (11) (12) are in between two Ir atoms. Moreover, switching from α-Li_2IrO_3 to $H_3LiIr_2O_6$ the octahedra get distorted in such a way the Li-O (2) (3) (5) (6) bonds and the Ir-O (8) (9) (10) (11) bonds become larger, whereas the Li-O (4) (5) bonds and the Ir-O (7) (10) become shorter.

In VASP, the relaxed structure of α-Li_2IrO_3 is highly anisotropic: all the atomic distances are different from each other and there is no symmetry. This distortion of the octahedra makes the honeycomb lattice formed by Ir atoms to be not perfectly symmetric and it could lift the degeneracy of the GS. The relaxed structure of $H_3LiIr_2O_6$ is instead very similar to the one produced with QE.

In all the previous cases, the perfect honeycomb symmetry of the Ir network is lost, meaning that α-Li_2IrO_3 and $H_3LiIr_2O_6$ show a structural instability (more evident in the case of α-Li_2IrO_3).

The Brillouin zone and the respective high symmetry points for Na_2IrO_3, α-Li_2IrO_3 and $H_3LiIr_2O_6$ are computed by using the online distribution AFLOW [21] and are reported in Fig.3.7. We consider the path along the high symmetry points reported in Tab.3.4, where k_i the i-th reduced coordinate (i.e. in units of $2\pi/a$) in the direct space basis $\{x, y, z\}$.

The electronic bands and the DOS of the non magnetic Na_2IrO_3, α-Li_2IrO_3 and $H_3LiIr2O_6$ are shown in Fig.3.8; the Fermi level is denoted with E_f. It turns out that at the Fermi level α-Li_2IrO_3 shows a vanishing DOS, whereas Na_2IrO_3 and $H_3LiIr_2O_6$ not. Then, we can already expect that in α-Li_2IrO_3 it will be unlikely to stabilize a magnetic order. Indeed, according to the Stoner criterion (formulated for a simple ferromagnet), a system prefers to be non magnetic if $DOS(E_f)U < 1$. Therefore, the large is the

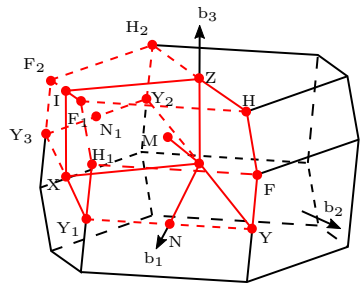

Figure 3.7: Brillouin zone and high symmetry paths for Na_2IrO_3, α-Li_2IrO_3 and $H_3LiIr_2O_6$.

#	Point	k_x	k_y	k_z
1	Γ	0.0	0.0	0.0
2	X	0.5	-0.5	0.0
3	I	0.5	-0.5	0.5
4	Z	0.0	0.0	0.5
5	Γ	0.0	0.0	0.0

Table 3.4: Path in reciprocal space for electronic computation.

DOS at the Fermi level, the easier is to stabilize finite magnetic moments.

3.3 Magnetic Relax DFT Calculations

We now compare the various ferromagnetic and anti-ferromagnetic spin configurations in Na_2IrO_3, α-Li_2IrO_3 and $H_3LiIr_2O_6$, in order to determine which magnetic configuration is the lowest energy one for each material. Therefore, we perform a relax magnetic calculation imposing a starting magnetization on the Ir atoms for the ferromagnetic and anti-ferromagnetic Néel, stripy, zigzag orderings (Fig.3.9). In order to initialize an anti-ferromagnetic spin configuration, we clearly need to distinguish two kind of Ir atoms: the ones with up magnetization and the ones with down magnetization. In the cases of stripy and zigzag ordering, one has to consider a structure made by two primitive cells in order to properly initialize the magnetic configuration. As initial magnetization, we consider moments with modulus 1/2 initialized along the **y** direction.

We perform a collinear calculation in QE and a non collinear calculation in VASP. Indeed, in VASP the collinear calculation accounts only for the magnetization along the **x** direction, but moments will be more likely to survive along the **y** direction, since they are initialized along **y**. We set up the terminology calling:

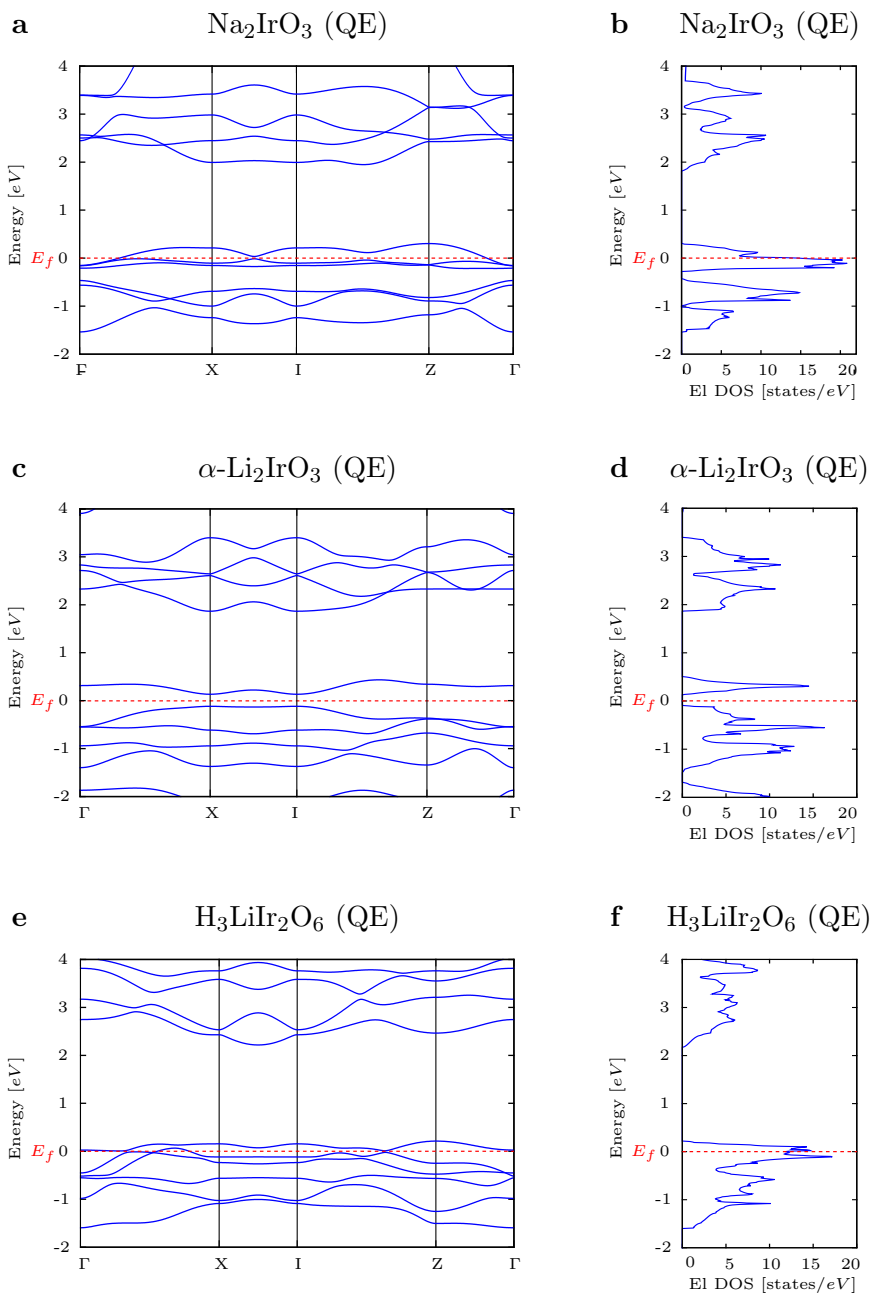

Figure 3.8: **a**, Electronic bands (QE) of non magnetic Na_2IrO_3. **b**, Electronic DOS (QE) of non magnetic Na_2IrO_3. **c**, Electronic bands (QE) of non magnetic α-Li_2IrO_3. **d**, Electronic DOS (QE) of non magnetic α-Li_2IrO_3. **e**, Electronic bands (QE) of non magnetic $H_3LiIr_2O_6$. **f**, Electronic DOS (QE) of non magnetic $H_3LiIr_2O_6$.

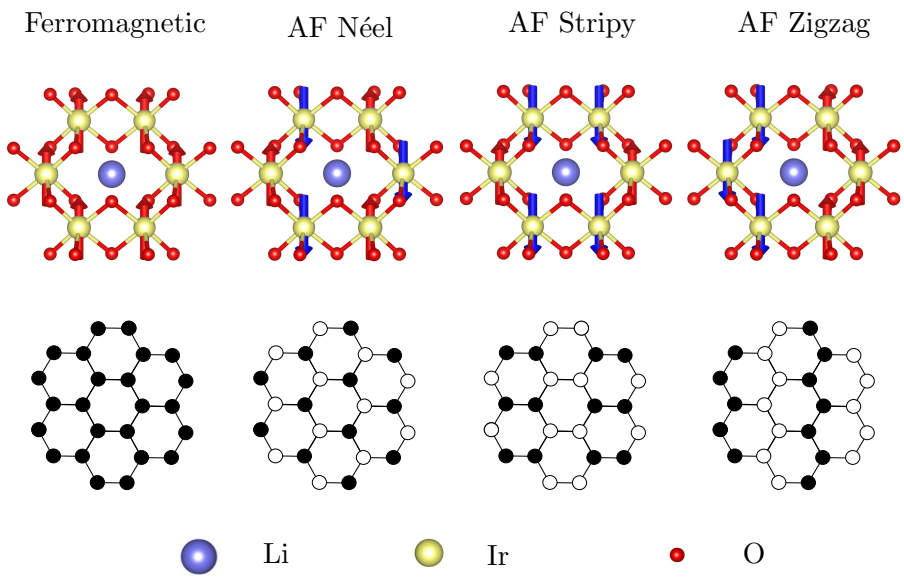

Figure 3.9: Ferromagnetic and anti-ferromagnetic orderings for Ir honeycomb layers.

- Stable those configurations for which a finite magnetization per Ir atom is still present at the end of the variable cell relax magnetic calculation.

- Unstable those configurations for which the initial magnetization on Ir atoms collapses to zero during the variable cell relax magnetic calculation (they will be denoted in the plots by ✕✕✕).

It is important to remark that this concept of stability is not related to the concept of instability that we have introduced before. It refers to whether it is possible or not to have a magnetic solution with a certain spins pattern and not to the lifting of the degeneracy of the GS configurations.

The comparisons of total energies and final magnetizations for the various magnetic orderings in Na_2IrO_3, α-Li_2IrO_3 and $H_3LiIr_2O_6$ are shown in Fig.3.10 and in Fig. 3.11; we denote with E_{tot}^{nm} the total energy of the non magnetic configuration.

For the QE simulation, it turns out that:

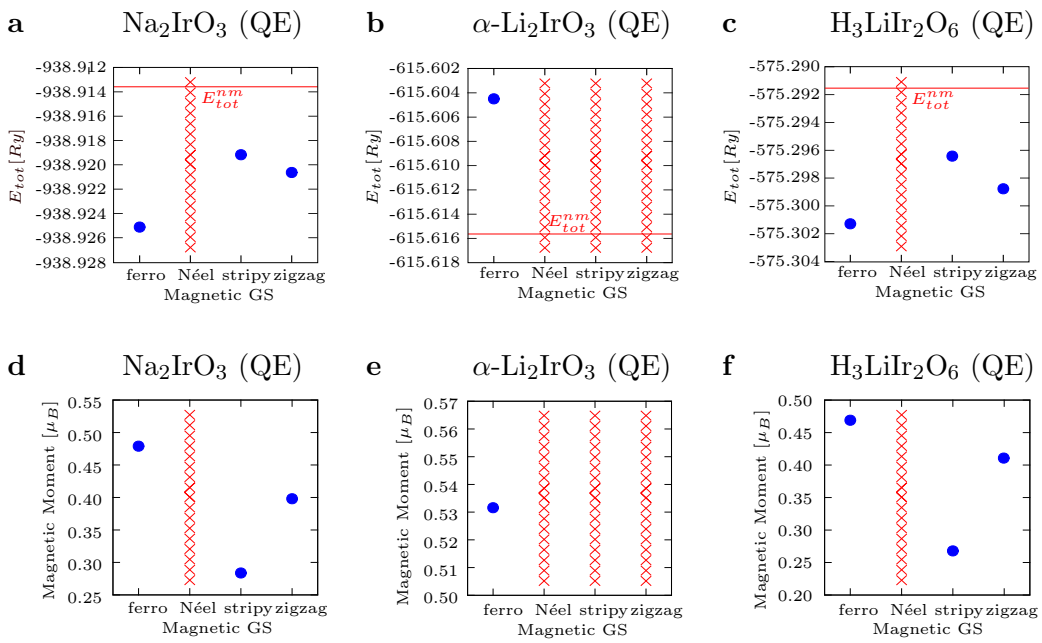

Figure 3.10: **a**, GS energy (QE) for 12 atoms unit cell of the various magnetic configurations in Na_2IrO_3. **b**, GS energy (QE) for 12 atoms unit cell of the various magnetic configurations in α-Li_2IrO_3. **c**, GS energy (QE) for 12 atoms unit cell of the various magnetic configurations in $H_3LiIr_2O_6$. **d**, Absolute value of the final magnetization per Ir atom (QE) of the various magnetic configurations in Na_2IrO_3. **e**, Absolute value of the final magnetization per Ir atom (QE) of the various magnetic configurations in α-Li_2IrO_3. **f**, Absolute value of the final magnetization per Ir atom (QE) of the various magnetic configurations in $H_3LiIr_2O_6$.

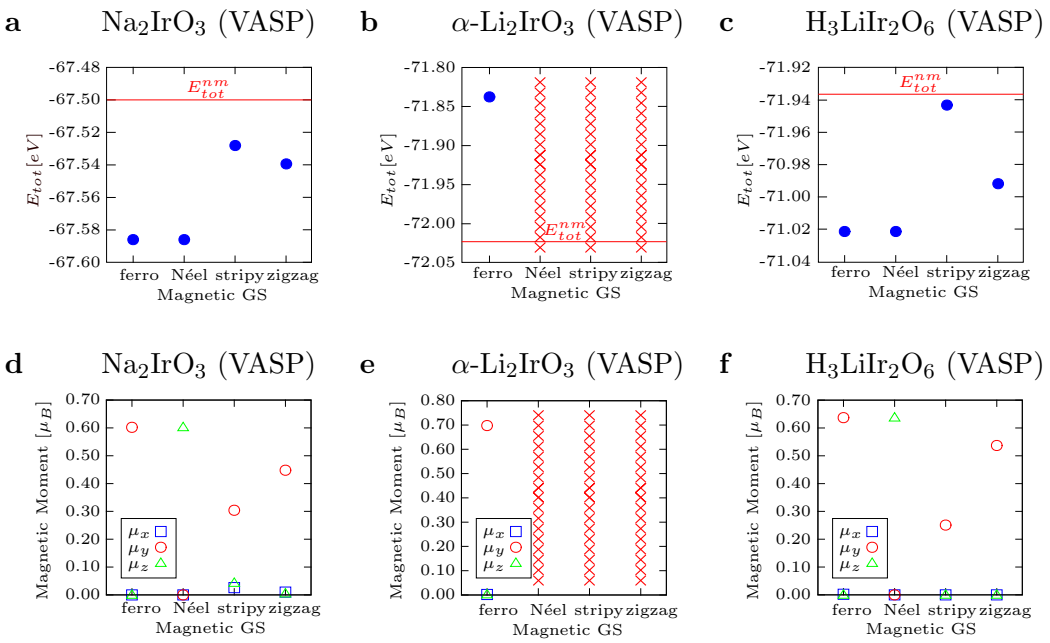

Figure 3.11: **a**, GS energy (VASP) for 12 atoms unit cell of the various magnetic configurations in Na_2IrO_3. **b**, GS energy (VASP) for 12 atoms unit cell of the various magnetic configurations in α-Li_2IrO_3. **c**, GS energy (VASP) for 12 atoms unit cell of the various magnetic configurations in $H_3LiIr_2O_6$. **d**, Absolute value of the final magnetization components per Ir atom (VASP) of the various magnetic configurations in Na_2IrO_3. **e**, Absolute value of the final magnetization components per Ir atom (VASP) of the various magnetic configurations in α-Li_2IrO_3. **f**, Absolute value of the final magnetization components per Ir atom (VASP) of the various magnetic configurations in $H_3LiIr_2O_6$.

- For Na_2IrO_3 it is possible to stabilize the ferromagnetic and the anti-ferrromagnetic zigzag and stripy configurations, but not the Néel order. Among the stable configurations, the ferromagnetic order is the preferred one and it is characterized by a larger magnetic moment than in the other two anti-ferromagnetic orderings. This is in contrast with respect to the experimental result, which instead reveals an anti-ferromagnetic zigzag order. Nevertheless, among the stable anti-ferromagnetic configurations, the zigzag order is the lowest energy one.

- For α-Li_2IrO_3 it is possible to stabilize only the ferromagnetic order and none of the anti-ferromagnetic configurations. This is related to the fact that the DOS at the Fermi level is zero.

- For $H_3LiIr_2O_6$ the situation is quite similar to the case of Na_2IrO_3. The anti-ferromagnetic Néel configuration does not stabilize and the ferromagnetic order is the lowest energy configuration.

We therefore notice that within QE the Néel magnetic ordering cannot be stabilized in all the three materials.

In VASP the picture is quite similar to the one found in QE with moments aligned mostly in the **y** direction, with exception of the anti-ferromagnetic Néel configuration. Indeed, not only it that can be stabilized in Na_2IrO_3 and in $H_3LiIr_2O_6$, but it is almost degenerate with the ferromagnetic configuration and it shows moments along the **x** direction rather than along the **y** direction.

Moreover, both QE and VASP agree on the presence of a magnetic instability for Na_2IrO_3 and $H_3LiIr_2O_6$, since the energy of the magnetic configurations is lower than the energy of the non magnetic configuration. This instability does not occur in α-Li_2IrO_3, where the non magnetic solution has still lower energy than the ferromagnetic one.

Then, we compute the electronic DOS in QE for the various stable magnetic configurations and compare them together with the non magnetic case. The results are shown in Fig.3.12.

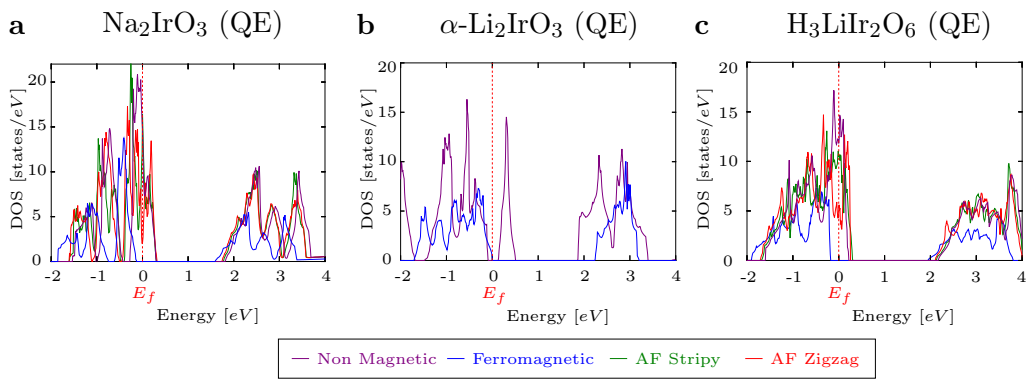

Figure 3.12: **a**, DOS (QE) of stable magnetic configurations in Na_2IrO_3. **b**, DOS (QE) of stable magnetic configurations in α-Li_2IrO_3. **c**, DOS (QE) of stable magnetic configurations in $H_3LiIr_2O_6$.

In all the three cases the behaviour of the DOS at the Fermi level is unchanged for the anti-ferromagnetic configurations, while the ferromagnetic one makes exception. More precisely:

- In Na_2IrO_3 and in $H_3LiIr_2O_6$ the ferromagnetic DOS is zero at the Fermi energy, whereas the non magnetic, anti-ferromagnetic stripy and zigzag DOS are not vanishing at the Fermi energy.

- In α-Li_2IrO_3 the DOS vanishes almost at the Fermi energy, whereas the non magnetic DOS is zero for an energy interval around the Fermi energy.

Overall, we notice that simple DFT calculations show a bias towards the ferromagnetic configuration, that is easier to be stabilized and that shows an higher magnetic moment. Indeed, the ferromagnetic solution stabilizes even in α-Li_2IrO_3, which is characterized by a zero DOS at the Fermi level. The inclusion of other effects, like U and/or SOC could play a big role and modify the above picture.

3.4 Non Magnetic DFT+U Calculations

We now include in our calculations the effect of the Coulomb repulsion U. We first look at the effect of U in the non magnetic Na_2IrO_3, α-Li_2IrO_3 and $H_3LiIr_2O_6$, before including it for the stable magnetic configurations. The behaviour of the DOS as function of U computed with QE is reported in Fig.3.13. We notice that as U increases the DOS shifts towards lower

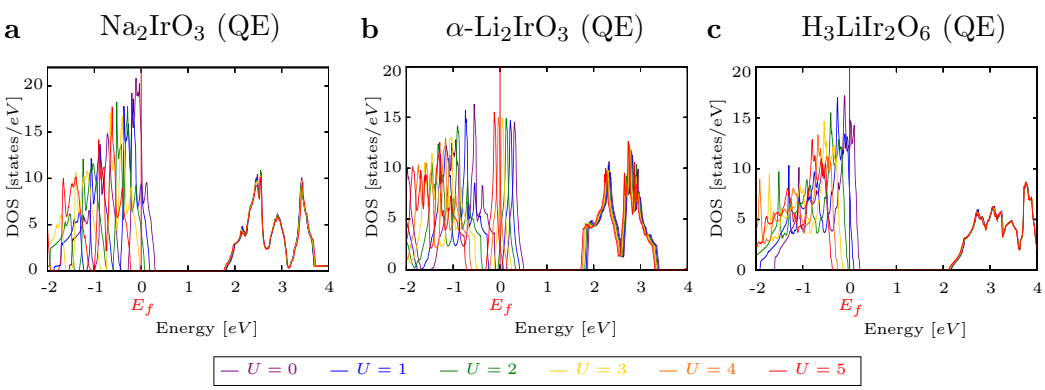

Figure 3.13: **a**, DOS (QE) for different values of the Coulomb repulsion U in Na_2IrO_3. **b**, DOS (QE) for different values of the Coulomb repulsion U in α-Li_2IrO_3. **c**, DOS (QE) for different values of the Coulomb repulsion U in $H_3LiIr_2O_6$.

energies; moreover the DOS below the Fermi level is much more affected by U rather that the DOS above the Fermi level. This implies that the energy gap increases as U increases and that the behaviour at the Fermi level can change. In particular:

- Na_2IrO_3 shows non zero DOS for $U \lesssim 3eV$.
- α-Li_2IrO_3 shows non zero DOS for $U \gtrsim 1.5eV$.
- $H_3LiIr_2O_6$ shows non zero DOS for $U \lesssim 1.7eV$.

3.5 Magnetic DFT+U Calculations

We are now interested in studying what happens to the magnetic configurations in presence of the Coulomb repulsion U. Considering the results in Fig.3.13, we study the effect of U in the range $[0eV, 3eV]$. We also check whether the presence of U allows some non stable magnetic configurations to stabilize.

The comparisons of total energies and final magnetizations within QE for the various magnetic orderings in Na_2IrO_3, α-Li_2IrO_3 and $H_3LiIr_2O_6$ with $U = 1.5eV$ and $U = 3eV$ are shown respectively in Fig.3.14 and Fig.3.15. It turns out that the presence of U is not able to make the previously unstable configurations to become stable (Néel in Na_2IrO_3; Néel, stripy and zigzag in α-Li_2IrO_3; Néel in $H_3LiIr_2O_6$.). Moreover, we find again that Na_2IrO_3 and $H_3LiIr_2O_6$ show a magnetic instability, whereas α-Li_2IrO_3 not. Additionally, the bias towards the ferromagnetic solution is still present even in presence of U: the ferromagnetic configuration is more stable than the anti-ferromagnetic configurations and the magnetic moments are larger.

A comparison between the electronic bands and DOS in absence and in presence of U for the various stable magnetizations within QE is reported in Fig.3.18, Fig.3.16 and Fig.3.17. We find that in presence of U the bands above the Fermi level are shifted towards higher energy, whereas the bands below the Fermi level are shifted towards lower energies. This effect is less evident for the bands near the Fermi level, implying that the behaviour at the Fermi level is not varied by the presence of U. This is in contrast to what we have found for the non magnetic case, where U was indeed able to modify the picture at the Fermi level and explains why it is not possible still to stabilize the unstable solutions in presence of U.

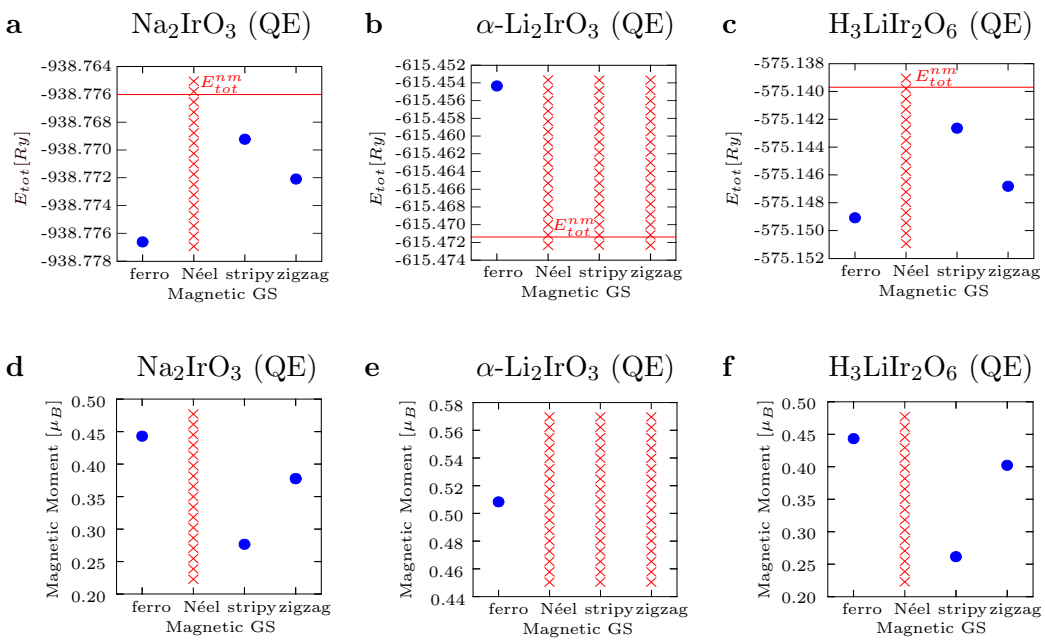

Figure 3.14: **a**, GS energy (QE) for 12 atoms unit cell of the various magnetic configurations in Na_2IrO_3 with $U = 1.5eV$. **b**, GS energy (QE) for 12 atoms unit cell of the various magnetic configurations in α-Li_2IrO_3 with $U = 1.5eV$. **c**, GS energy (QE) for 12 atoms unit cell of the various magnetic configurations in $H_3LiIr_2O_6$ with $U = 1.5eV$. **d**, Absolute value of the final magnetization per Ir atom (QE) of the various magnetic configurations in Na_2IrO_3 with $U = 1.5eV$. **e**, Absolute value of the final magnetization per Ir atom (QE) of the various magnetic configurations in α-Li_2IrO_3 with $U = 1.5eV$. **f**, Absolute value of the final magnetization per Ir atom (QE) of the various magnetic configurations in $H_3LiIr_2O_6$ with $U = 1.5eV$.

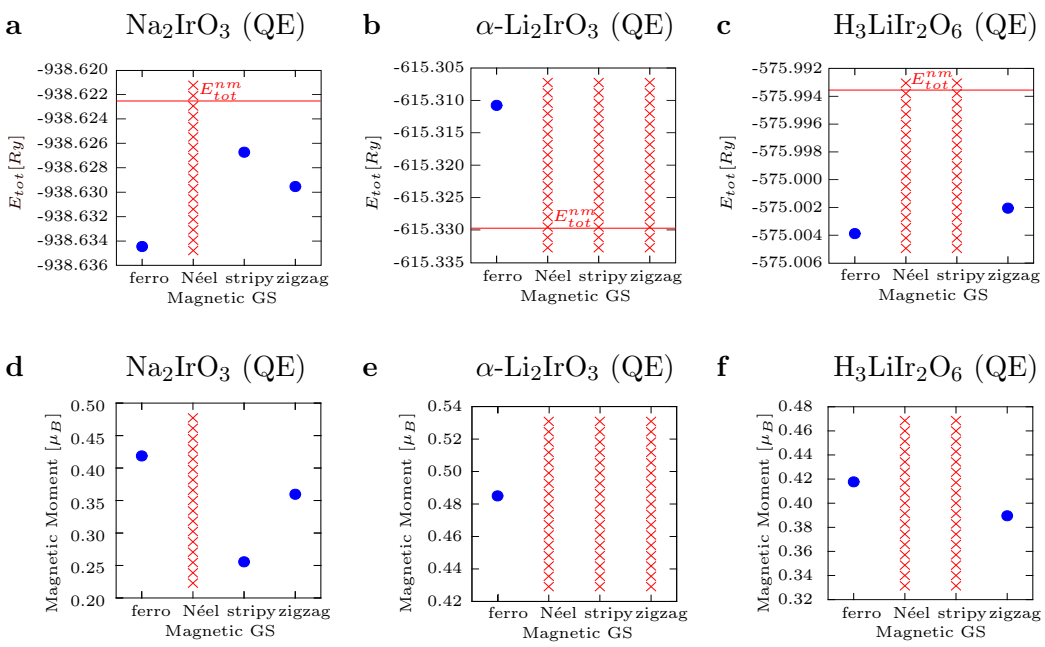

Figure 3.15: **a**, GS energy (QE) for 12 atoms unit cell of the various magnetic configurations in Na_2IrO_3 with $U = 3eV$. **b**, GS energy (QE) for 12 atoms unit cell of the various magnetic configurations in α-Li_2IrO_3 with $U = 3eV$. **c**, GS energy (QE) for 12 atoms unit cell of the various magnetic configurations in $H_3LiIr_2O_6$ with $U = 3eV$. **d**, Absolute value of the final magnetization per Ir atom (QE) of the various magnetic configurations in Na_2IrO_3 with $U = 3eV$. **e**, Absolute value of the final magnetization per Ir atom (QE) of the various magnetic configurations in α-Li_2IrO_3 with $U = 3eV$. **f**, Absolute value of the final magnetization per Ir atom (QE) of the various magnetic configurations in $H_3LiIr_2O_6$ with $U = 3eV$.

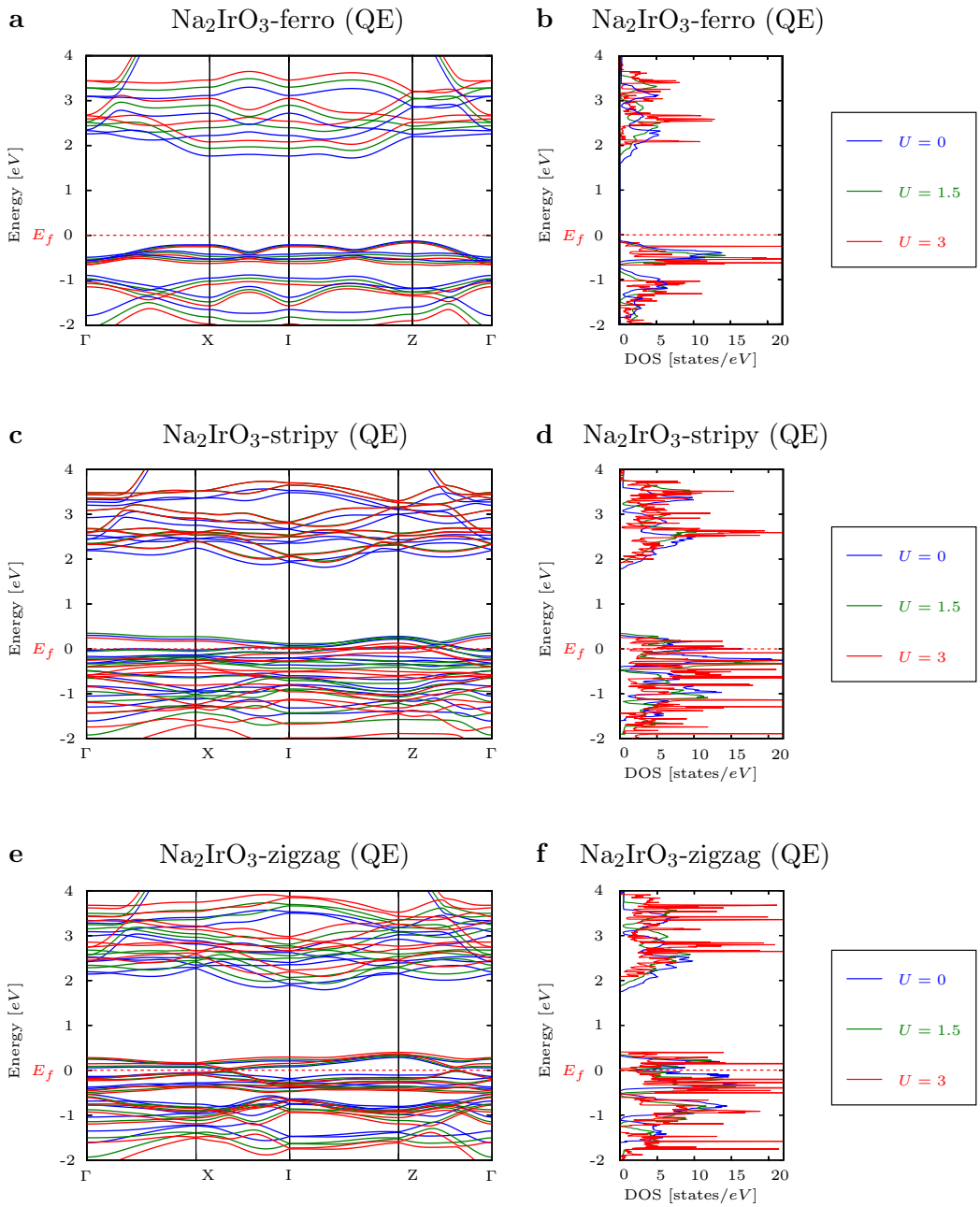

Figure 3.16: **a**, Electronic bands (QE) of ferromagnetic Na_2IrO_3. **b**, Electronic DOS (QE) of ferromagnetic Na_2IrO_3. **c**, Electronic bands (QE) of anti-ferromagnetic stripy Na_2IrO_3. **d**, Electronic DOS (QE) of anti-ferromagnetic stripy Na_2IrO_3. **e**, Electronic bands (QE) of anti-ferromagnetic zigzag Na_2IrO_3. **f**, Electronic DOS (QE) of anti-ferromagnetic zigzag Na_2IrO_3.

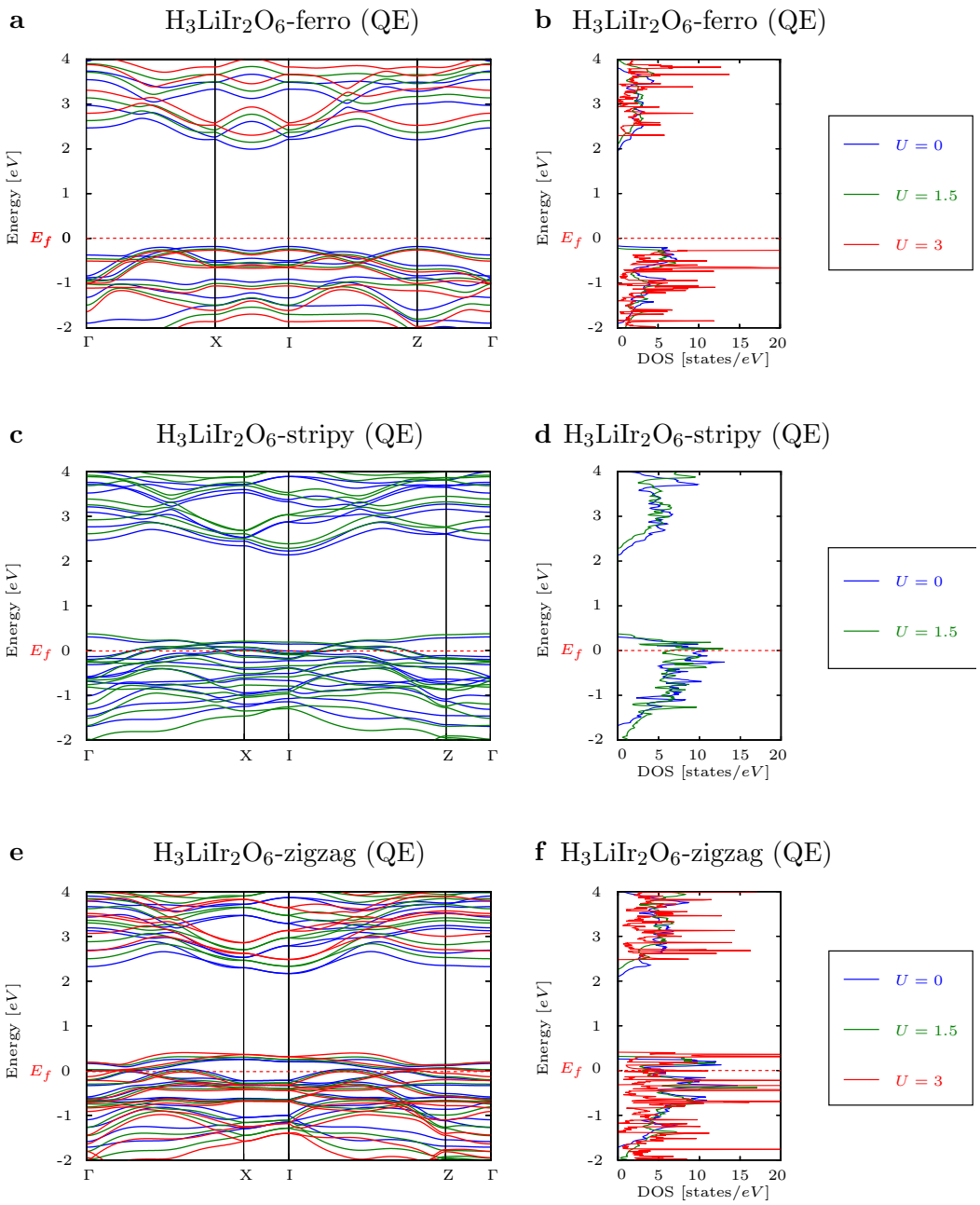

Figure 3.17: **a**, Electronic bands (QE) of ferromagnetic $H_3LiIr_2O_6$. **b**, Electronic DOS (QE) of ferromagnetic $H_3LiIr_2O_6$. **c**, Electronic bands (QE) of anti-ferromagnetic stripy $H_3LiIr_2O_6$. **d**, Electronic DOS (QE) of anti-ferromagnetic stripy $H_3LiIr_2O_6$. **e**, Electronic bands (QE) of anti-ferromagnetic zigzag $H_3LiIr_2O_6$. **f**, Electronic DOS (QE) of anti-ferromagnetic zigzag $H_3LiIr_2O_6$.

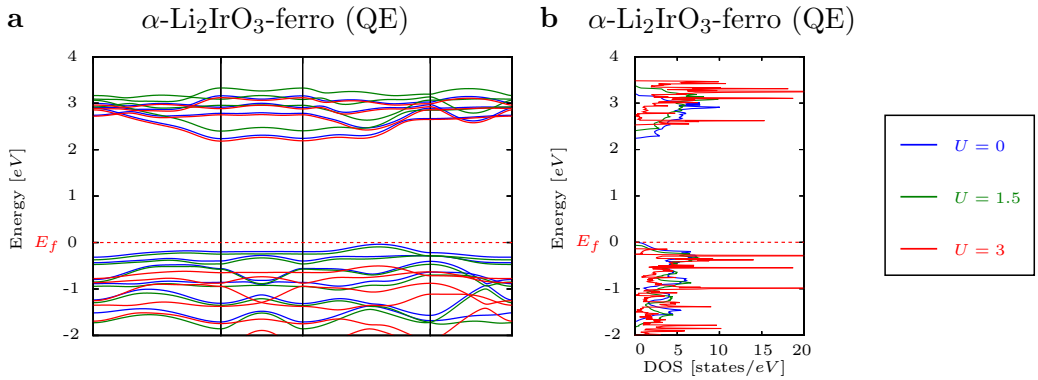

Figure 3.18: **a**, Electronic bands (QE) of ferromagnetic α-Li_2IrO_3. **b**, Electronic DOS (QE) of ferromagnetic α-Li_2IrO_3.

3.6 Magnetic DFT+*SOC* Calculations

We now insert also *SOC* in our simulations. It turns out that within QE, calculations do not converge. On the other hand, with VASP we get the results shown in Fig. 3.19. The picture is quite different with respect to the case without *SOC* (Fig.3.11). Indeed, we have that:

- In Na_2IrO_3 the anti-ferromagnetic Néel configuration becomes more stable than the other magnetic patterns, but on the other hand it shows lower values of magnetic moments than in absence of *SOC*. Moreover, the magnetic moments align mostly along the **x** direction, whereas in absence of *SOC* they were mostly aligned along the **y** direction.

- In α-Li_2IrO_3 it is possible to stabilize the anti-ferromagnetic configurations, even if the value of the magnetic moments is very low. Also in this case, the anti-ferromagnetic Néel configuration dominates with respect to the other magnetic configurations.

- In $H_3LiIr_2O_6$ the anti-ferromagnetic zigzag becomes the most stable configuration, but it shows lower magnetic moments rather than in absence of *SOC*. Also in this case, the directions of the magnetic moments change a lot with respect to the case in absence of *SOC*.

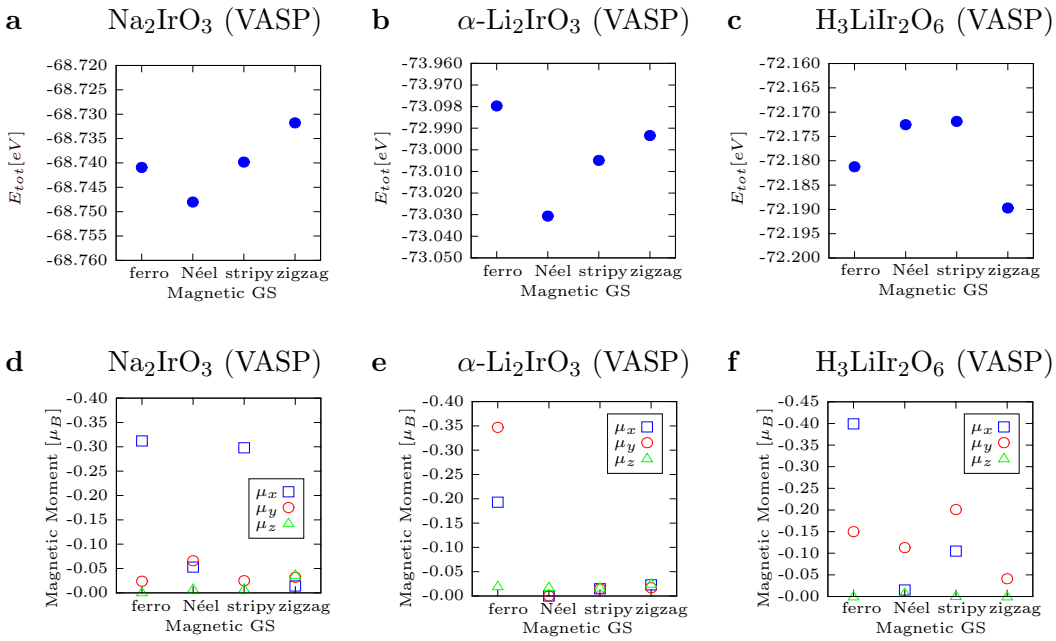

Figure 3.19: **a**, GS energy (VASP) for 12 atoms unit cell of the various magnetic configurations in Na_2IrO_3 in presence of *SOC*. **b**, GS energy (VASP) for 12 atoms unit cell of the various magnetic configurations in α-Li_2IrO_3 in presence of *SOC*. **c**, GS energy (VASP) for 12 atoms unit cell of the various magnetic configurations in $H_3LiIr_2O_6$ in presence of *SOC*. **d**, Absolute value of the final magnetization components per Ir atom (VASP) of the various magnetic configurations in Na_2IrO_3 in presence of *SOC*. **e**, Absolute value of the final magnetization components per Ir atom (VASP) of the various magnetic configurations in α-Li_2IrO_3 in presence of *SOC*. **f**, Absolute value of the final magnetization components per Ir atom (VASP) of the various magnetic configurations in $H_3LiIr_2O_6$ in presence of *SOC*.

3.7 Magnetic DFT+SOC+U Calculations

We finally try to insert U (in the range $[0eV, 3eV]$) and SOC together for the various ferromagnetic and anti-ferromagnetic orderings in Na_2IrO_3, α-Li_2IrO_3 and $H_3LiIr_2O_6$, but in both QE and VASP calculations do not converge. Still, the simultaneous inclusion of SOC and U might be essential to find the proper competition between magnetic orderings. Indeed, in the case of Na_2IrO_3 we would expect the anti-ferromagnetic zigzag order to be the lowest energy one since this is what it is found experimentally, but this is not the case if we consider U and SOC applied only separately.

Chapter 4

Conclusions

Our work has been focused on the computational study of the structural, electronic and magnetic properties of the honeycomb iridates Na_2IrO_3, α-Li_2IrO_3 and $H_3LiIr_2O_6$ by performing DFT calculations, including the Coulomb repulsion U and/or spin orbit coupling (SOC), with the codes QUANTUM ESPRESSO and VASP.

First we have reproduced all the allowed theoretical structures for α-Li_2IrO_3 and $H_3LiIr_2O_6$, by considering the possible stacking patterns of their layers. For each of these structures, we carried out a variable-cell relax calculation and compared the electronic ground state energies of all these structures in order to find the lowest energy configurations for each material, which turned out to be in agreement with the experimental observations. Moreover, by looking at the atomic distances in the lowest energy structures, we highlighted that a structural instability occurs, because of the distortion of the Ir network from the perfect honeycomb lattice. Next, we considered only the lowest energy structures for each material for successive calculations.

We then focused on the magnetic properties of Na_2IrO_3, α-Li_2IrO_3 and $H_3LiIr_2O_3$ by performing DFT calculations with a starting magnetization on the Ir atoms, to reproduce the ferromagnetic order and the Néel, stripy and zigzag anti-ferromagnetic orderings. We found that some configurations are unstable, meaning that the initial magnetic moments collapse to zero

during the DFT calculation. Among the configurations in which magnetic moments survive, Na_2IrO_3 and $H_3LiIr_2O_6$ show a magnetic instability, since the magnetic configurations have lower energy than the non magnetic one. This behaviour does not occur instead in α-Li_2IrO_3, where the energy is lower in the non magnetic rather than in the magnetic configurations.

Then, we inserted the Coulomb repulsion U and we noticed that it controls the value of the DOS at the Fermi level, from being zero to non vanishing, for the non magnetic configurations in the three materials. According to the Stoner criterion, this implies a variation in the tendency of the system to be magnetic and, therefore, it could be crucial in stabilizing the magnetic configurations that are unstable in absence of U. Nevertheless, the inclusion of U in DFT calculations does not change the behaviour of the DOS at the Fermi level in magnetic configurations and, indeed, the unstable configurations in absence of U remain unstable even in presence of U.

Additionally, we carried out calculations with SOC and we found not only that the initial moments do not vanish in any magnetic configuration, but also that the competition between the total energies for the various magnetic orderings radically changes when accounting for SOC.

Finally, we performed calculations with simultaneous presence of SOC and U but they did not converge. Still, the simultaneous inclusion of SOC and U might be essential to find the proper competition between the energies of the various magnetic orderings, in order to reproduce results closer to experimental data. Therefore, next study directions would be to make DFT+U calculations converge in presence of SOC and then to study the phononic properties of Na_2IrO_3, α-Li_2IrO_3 and $H_3LiIr_2O_6$, in order to spot the possible occurrence of phononic instabilities.

Appendix A

Convergence Tests

In running simulations, one should carefully choose a good set of parameters that allows calculations to converge. In this sense, the parameters that play a crucial role are:

- E_{cut}: energy cut-off for plane wave expansion.
- $\mathbf{k}_{grid}$: Monkhorst-Pack grid.
- δ_{gauss}: Marzari-Vanderbilt smearing.

In particular, E_{cut} controls the number of plane waves that are used in the calculation; the more they are, the more the results are precise but, on the other hand, the higher is the computational cost. Similarly, the finer is the Monkhorst-Pack grid and the smaller is the smearing, the more the results are precise but the heavier are the calculations. Clearly, a finer grid requires a smaller smearing in order to have an appreciable effect on the results. Generally, one chooses the values of these parameters by performing convergence tests for the non magnetic solution without U and SOC, that means looking at the behaviour of the total energy of the system as function of the parameters. The convergence is usually considered for a change in the total energy less than $1eV$. We fix $\delta_{gauss} = 10^{-6}$ and we let E_{cut} and $\mathbf{k}_{grid}$ vary.

The convergence tests for E_{cut} and $\mathbf{k}_{grid}$ in QE are reported in Fig.A.1. We notice that $\mathbf{k}_{grid}$ does not play a big role in determining the value of E_{tot}, then we may choose in principle $\mathbf{k}_{grid} = (8, 8, 8)$. Still, we prefer to use $\mathbf{k}_{grid} = (12, 12, 12)$ to be as precise as possible and help calculations to converge more easily. On the other hand, E_{cut} affects the value of E_{tot} more; for $E_{cut} \geq 80Ry$, the change in the total energy is sufficiently small and therefore we may choose $E_{cut} = 80eV$ for our calculations.

The convergence tests for E_{cut} and $\mathbf{k}_{grid}$ in VASP are reported in Fig.A.2. Also in this case we notice that $\mathbf{k}_{grid}$ does not play a big role in determining the value of E_{tot}, whereas E_{cut} does. Then we may choose $\mathbf{k}_{grid} = (8, 8, 8)$ and $E_{cut} = 600eV$, above which the total energy fluctuations do not decrease.

Those convergence calculations lead us to choose the set of parameters shown in Tab.3.1.

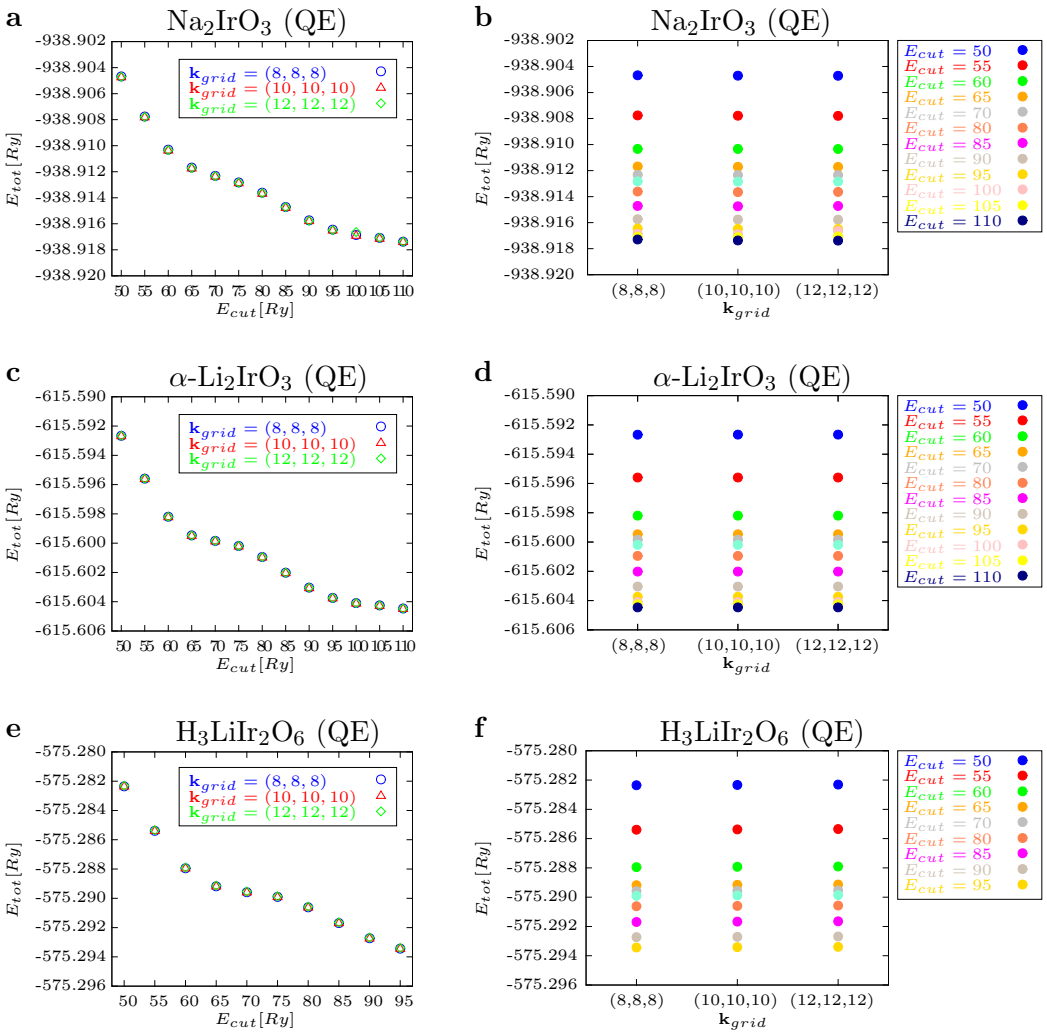

Figure A.1: **a**, Convergence test (QE) for E_{cut} in Na_2IrO_3. **b**, Convergence test (QE) for $\mathbf{k}_{grid}$ in Na_2IrO_3. **c**, Convergence test (QE) for E_{cut} in α-Li_2IrO_3. **d**, Convergence test (QE) for $\mathbf{k}_{grid}$ in α-Li_2IrO_3. **e**, Convergence test (QE) for E_{cut} in $H_3LiIr_2O_6$. **f**, Convergence test (QE) for $\mathbf{k}_{grid}$ in $H_3LiIr_2O_6$.

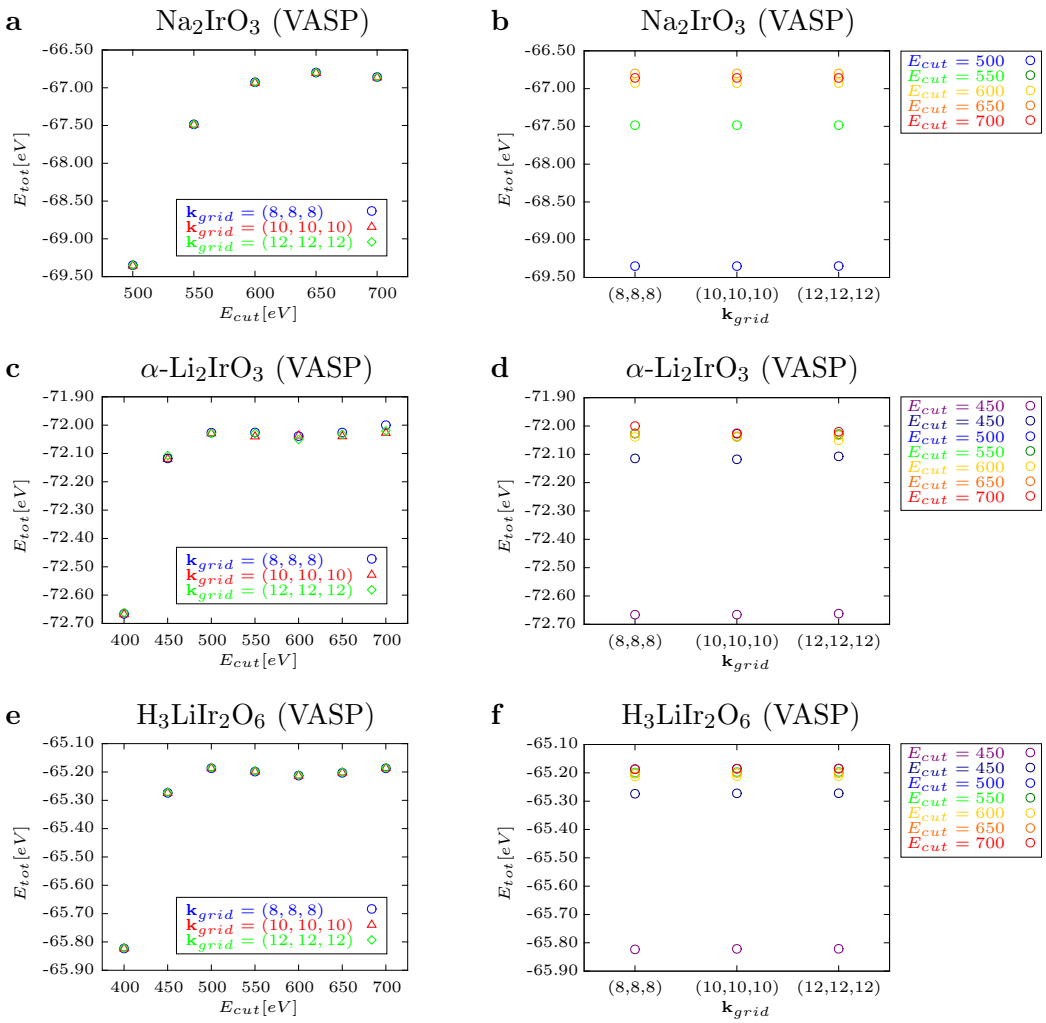

Figure A.2: **a**, Convergence test (VASP) for E_{cut} in Na_2IrO_3. **b**, Convergence test (VASP) for $\mathbf{k}_{grid}$ in Na_2IrO_3. **c**, Convergence test (VASP) for E_{cut} in α-Li_2IrO_3. **d**, Convergence test (VASP) for $\mathbf{k}_{grid}$ in α-Li_2IrO_3. **e**, Convergence test (VASP) for E_{cut} in $H_3LiIr_2O_6$. **f**, Convergence test (VASP) for $\mathbf{k}_{grid}$ in $H_3LiIr_2O_6$.

Appendix B

Allowed Structures for Honeycomb Iridates

In Tabs.B.1 B.2 B.3 B.4 we report the initial atomic coordinates and lattice vectors $\mathbf{v}_i$ $(i = 1, 2, 3)$ generated within the framework of the Pymatgen library for the various stackings, as discussed in 3.1. Those initial structures are the same for Na_2IrO_3, Li_2IrO_3 and $H_3LiIr_2O_6$, what only changes are the atomic species occupying the various sites. We denote with A the intralayer atom type and with I the interlayer atom type. Then, we have that:

- Na_2IrO_3: A = Na, I = Na
- α-Li_2IrO_3: A = Li, I = Li
- $H_3LiIr_2O_6$: A = Li, I = H

The reduction to the primitive cell is performed using the Pymatgen function *IStructure.get_primitive_structure*. Some stackings allow for a smaller primitive cell, whereas other stackings require a larger primitive cell.

Stacking O3-ACB			
Atom	x	y	z
I	0.250000	0.250000	0.333333
I	0.250000	0.583333	0.666667
I	0.250000	0.916667	1.000000
Ir	0.750000	0.750000	0.333333
Ir	0.750000	0.083333	0.666667
A	0.750000	0.416667	1.000000
O	0.000000	1.000000	0.333333
O	0.000000	0.333333	0.666667
O	1.000000	0.666667	1.000000
O	0.500000	0.166667	1.000000
O	0.500000	0.500000	0.333333
O	0.500000	0.833333	0.666667
$\mathbf{v}_1 = (-1.7500001.010363 - 4.666667)$			
$\mathbf{v}_2 = (-5.2500003.031089 - 0.000000)$			
$\mathbf{v}_3 = (0.0000006.0621780.000000)$			

Stacking O3-BAC			
Atom	x	y	z
I	0.250000	0.916667	0.333333
I	0.250000	0.250000	0.666667
I	0.250000	0.583333	1.000000
Ir	0.750000	0.750000	0.333333
Ir	0.750000	0.083333	0.666667
A	0.750000	0.416667	1.000000
O	0.000000	1.000000	0.333333
O	0.000000	0.333333	0.666667
O	1.000000	0.666667	1.000000
O	0.500000	0.166667	1.000000
O	0.500000	0.500000	0.333333
O	0.500000	0.833333	0.666667
$\mathbf{v}_1 = (-1.7500001.010363 - 4.666667)$			
$\mathbf{v}_2 = (-5.2500003.031089 - 0.000000)$			
$\mathbf{v}_3 = (0.0000006.0621780.000000)$			

Stacking O3-CBA			
Atom	x	y	z
I	0.250000	0.250000	1.000000
I	0.250000	0.583333	0.333333
I	0.250000	0.916667	0.666667
Ir	0.750000	0.750000	0.333333
Ir	0.750000	0.083333	0.666667
A	0.750000	0.416667	1.000000
O	0.000000	1.000000	0.333333
O	0.000000	0.333333	0.666667
O	1.000000	0.666667	1.000000
O	0.500000	0.166667	1.000000
O	0.500000	0.500000	0.333333
O	0.500000	0.833333	0.666667
$\mathbf{v}_1 = (-1.750000, 1.010363, -4.666667)$			
$\mathbf{v}_2 = (-5.250000, 3.031089, -0.000000)$			
$\mathbf{v}_3 = (0.000000, 6.062178, 0.000000)$			

Stacking O3-ACB			
Atom	x	y	z
I	0.333333	0.333333	0.250000
I	0.666667	0.000000	0.250000
I	1.000000	0.666667	0.250000
I	0.000000	0.000000	0.583333
I	0.333333	0.666667	0.583333
I	0.666667	0.333333	0.583333
I	0.333333	1.000000	0.916667
I	0.666667	0.666667	0.916667
I	0.000000	0.333333	0.916667
Ir	0.333333	1.000000	0.083333
Ir	0.666667	0.666667	0.083333
Ir	0.333333	0.666667	0.416667
Ir	0.666667	0.333333	0.416667
Ir	0.333333	0.333333	0.750000
Ir	0.666667	0.000000	0.750000
A	0.000000	0.333333	0.083333
A	0.000000	0.000000	0.416667
A	1.000000	0.666667	0.750000
O	0.333333	0.333333	0.000000
O	0.666667	0.000000	0.000000
O	1.000000	0.666667	0.000000
O	0.000000	0.000000	0.166667
O	0.333333	0.666667	0.166667
O	0.666667	0.333333	0.166667
O	0.333333	1.000000	0.333333
O	0.666667	0.666667	0.333333
O	0.000000	0.333333	0.333333
O	0.333333	0.333333	0.500000
O	0.666667	0.000000	0.500000
O	1.000000	0.666667	0.500000
O	0.000000	0.000000	0.666667
O	0.333333	0.666667	0.666667
O	0.666667	0.333333	0.666667
O	0.333333	1.000000	0.833333
O	0.666667	0.666667	0.833333
O	0.000000	0.333333	0.833333
$\mathbf{v}_1 = (5.250000, 3.031089, 0.000000)$			
$\mathbf{v}_2 = (-5.250000, 3.031089, -0.000000)$			
$\mathbf{v}_3 = (-0.000000, -0.000000, 14.000000)$			

Stacking O3-BCA			
Atom	x	y	z
I	0.000000	0.000000	0.250000
I	0.333333	0.666667	0.250000
I	0.666667	0.333333	0.250000
I	0.333333	1.000000	0.583333
I	0.666667	0.666667	0.583333
I	0.000000	0.333333	0.583333
I	0.333333	0.333333	0.916667
I	0.666667	0.000000	0.916667
I	1.000000	0.666667	0.916667
Ir	0.333333	1.000000	0.083333
Ir	0.666667	0.666667	0.083333
Ir	0.333333	0.666667	0.416667
Ir	0.666667	0.333333	0.416667
Ir	0.333333	0.333333	0.750000
Ir	0.666667	0.000000	0.750000
A	0.000000	0.333333	0.083333
A	0.000000	0.000000	0.416667
A	1.000000	0.666667	0.750000
O	0.333333	0.333333	0.000000
O	0.666667	0.000000	0.000000
O	1.000000	0.666667	0.000000
O	0.000000	0.000000	0.166667
O	0.333333	0.666667	0.166667
O	0.666667	0.333333	0.166667
O	0.333333	1.000000	0.333333
O	0.666667	0.666667	0.333333
O	0.000000	0.333333	0.333333
O	0.333333	0.333333	0.500000
O	0.666667	0.000000	0.500000
O	1.000000	0.666667	0.500000
O	0.000000	0.000000	0.666667
O	0.333333	0.666667	0.666667
O	0.666667	0.333333	0.666667
O	0.333333	1.000000	0.833333
O	0.666667	0.666667	0.833333
O	0.000000	0.333333	0.833333
$\mathbf{v}_1 = (5.250000, 3.031089, 0.000000)$			
$\mathbf{v}_2 = (-5.250000, 3.031089, -0.000000)$			
$\mathbf{v}_3 = (-0.000000, -0.000000, 14.000000)$			

Stacking O3-CAB			
Atom	x	y	z
I	0.333333	1.000000	0.250000
I	0.666667	0.666667	0.250000
I	0.000000	0.333333	0.250000
I	0.333333	0.333333	0.583333
I	0.666667	0.000000	0.583333
I	1.000000	0.666667	0.583333
I	0.000000	0.000000	0.916667
I	0.333333	0.666667	0.916667
I	0.666667	0.333333	0.916667
Ir	0.333333	1.000000	0.083333
Ir	0.666667	0.666667	0.083333
Ir	0.333333	0.666667	0.416667
Ir	0.666667	0.333333	0.416667
Ir	0.333333	0.333333	0.750000
Ir	0.666667	0.000000	0.750000
A	0.000000	0.333333	0.083333
A	0.000000	0.000000	0.416667
A	1.000000	0.666667	0.750000
O	0.333333	0.333333	0.000000
O	0.666667	0.000000	0.000000
O	1.000000	0.666667	0.000000
O	0.000000	0.000000	0.166667
O	0.333333	0.666667	0.166667
O	0.666667	0.333333	0.166667
O	0.333333	1.000000	0.333333
O	0.666667	0.666667	0.333333
O	0.000000	0.333333	0.333333
O	0.333333	0.333333	0.500000
O	0.666667	0.000000	0.500000
O	1.000000	0.666667	0.500000
O	0.000000	0.000000	0.666667
O	0.333333	0.666667	0.666667
O	0.666667	0.333333	0.666667
O	0.333333	1.000000	0.833333
O	0.666667	0.666667	0.833333
O	0.000000	0.333333	0.833333
$\mathbf{v}_1 = (5.250000, 3.031089, 0.000000)$			
$\mathbf{v}_2 = (-5.250000, 3.031089, -0.000000)$			
$\mathbf{v}_3 = (-0.000000, -0.000000, 14.000000))$			

Table B.1: Lattice parameters for the layer stacking O3.

Stacking P3-ABC			
Atom	x	y	z
I	0.250000	0.583333	0.666667
I	0.250000	0.250000	0.333333
I	0.250000	0.916667	1.000000
Ir	0.750000	0.416667	0.666667
Ir	0.750000	0.083333	0.333333
A	0.750000	0.750000	1.000000
O	0.000000	0.000000	0.666667
O	0.000000	0.666667	0.333333
O	1.000000	0.333333	0.000000
O	0.500000	0.166667	1.000000
O	0.500000	0.833333	0.666667
O	0.500000	0.500000	0.333333
$\mathbf{v}_1 = (1.750000, -1.010363, -4.666667)$			
$\mathbf{v}_2 = (5.250000, -3.031089, 0.000000)$			
$\mathbf{v}_3 = (0.000000, -6.062178, -0.000000)$			

Stacking P3-BCA			
Atom	x	y	z
I	0.250000	0.250000	1.000000
I	0.250000	0.916667	0.666667
I	0.250000	0.583333	0.333333
Ir	0.750000	0.416667	0.666667
Ir	0.750000	0.083333	0.333333
A	0.750000	0.750000	1.000000
O	0.000000	0.000000	0.666667
O	0.000000	0.666667	0.333333
O	1.000000	0.333333	0.000000
O	0.500000	0.166667	1.000000
O	0.500000	0.833333	0.666667
O	0.500000	0.500000	0.333333
$\mathbf{v}_1 = (1.750000, -1.010363, -4.666667)$			
$\mathbf{v}_2 = (5.250000, -3.031089, 0.000000)$			
$\mathbf{v}_3 = (0.000000, -6.062178, -0.000000)$			

Stacking P3-CAB			
Atom	x	y	z
I	0.250000	0.250000	0.666667
I	0.250000	0.916667	0.333333
I	0.250000	0.583333	1.000000
Ir	0.750000	0.416667	0.666667
Ir	0.750000	0.083333	0.333333
A	0.750000	0.750000	1.000000
O	0.000000	0.000000	0.666667
O	0.000000	0.666667	0.333333
O	1.000000	0.333333	0.000000
O	0.500000	0.166667	1.000000
O	0.500000	0.833333	0.666667
O	0.500000	0.500000	0.333333
$\mathbf{v}_1 = (1.750000, -1.010363, -4.666667)$			
$\mathbf{v}_2 = (5.250000, -3.031089, 0.000000)$			
$\mathbf{v}_3 = (0.000000, -6.062178, -0.000000)$			

Stacking P3-ACB			
Atom	x	y	z
I	0.333333	0.333333	0.250000
I	0.666667	0.000000	0.250000
I	1.000000	0.666667	0.250000
I	0.333333	1.000000	0.583333
I	0.666667	0.666667	0.583333
I	0.000000	0.333333	0.583333
I	0.000000	0.000000	0.916667
I	0.333333	0.666667	0.916667
I	0.666667	0.333333	0.916667
Ir	0.333333	1.000000	0.083333
Ir	0.666667	0.666667	0.083333
Ir	0.333333	0.333333	0.416667
Ir	0.666667	0.000000	0.416667
Ir	0.333333	0.666667	0.750000
Ir	0.666667	0.333333	0.750000
A	0.000000	0.333333	0.083333
A	1.000000	0.666667	0.416667
A	0.000000	0.000000	0.750000
O	0.333333	0.333333	0.000000
O	0.666667	0.000000	0.000000
O	1.000000	0.666667	0.000000
O	0.000000	0.000000	0.166667
O	0.333333	0.666667	0.166667
O	0.666667	0.333333	0.166667
O	0.000000	0.000000	0.333333
O	0.333333	0.666667	0.333333
O	0.666667	0.333333	0.333333
O	0.333333	1.000000	0.500000
O	0.666667	0.666667	0.500000
O	0.000000	0.333333	0.500000
O	0.333333	1.000000	0.666667
O	0.666667	0.666667	0.666667
O	0.000000	0.333333	0.666667
O	0.333333	0.333333	0.833333
O	0.666667	0.000000	0.833333
O	1.000000	0.666667	0.833333
$\mathbf{v}_1 = (5.250000, 3.031089, 0.000000)$			
$\mathbf{v}_2 = (-5.250000, 3.031089, -0.000000)$			
$\mathbf{v}_3 = (-0.000000, -0.000000, 14.000000)$			

Stacking P3-BAC			
Atom	x	y	z
I	0.000000	0.000000	0.250000
I	0.333333	0.666667	0.250000
I	0.666667	0.333333	0.250000
I	0.333333	0.333333	0.583333
I	0.666667	0.000000	0.583333
I	1.000000	0.666667	0.583333
I	0.333333	1.000000	0.916667
I	0.666667	0.666667	0.916667
I	0.000000	0.333333	0.916667
Ir	0.333333	1.000000	0.083333
Ir	0.666667	0.666667	0.083333
Ir	0.333333	0.333333	0.416667
Ir	0.666667	0.000000	0.416667
Ir	0.333333	0.666667	0.750000
Ir	0.666667	0.333333	0.750000
A	0.000000	0.333333	0.083333
A	1.000000	0.666667	0.416667
A	0.000000	0.000000	0.750000
O	0.333333	0.333333	0.000000
O	0.666667	0.000000	0.000000
O	1.000000	0.666667	0.000000
O	0.000000	0.000000	0.166667
O	0.333333	0.666667	0.166667
O	0.666667	0.333333	0.166667
O	0.000000	0.000000	0.333333
O	0.333333	0.666667	0.333333
O	0.666667	0.333333	0.333333
O	0.333333	1.000000	0.500000
O	0.666667	0.666667	0.500000
O	0.000000	0.333333	0.500000
O	0.333333	1.000000	0.666667
O	0.666667	0.666667	0.666667
O	0.000000	0.333333	0.666667
O	0.333333	0.333333	0.833333
O	0.666667	0.000000	0.833333
O	1.000000	0.666667	0.833333
$\mathbf{v}_1 = (5.250000, 3.031089, 0.000000)$			
$\mathbf{v}_2 = (-5.250000, 3.031089, -0.000000)$			
$\mathbf{v}_3 = (-0.000000, -0.000000, 14.000000)$			

Stacking P3-CBA			
Atom	x	y	z
I	0.333332966	0.000000000	0.250000000
I	0.666666976	0.666666996	0.250000000
I	0.000000016	0.333332998	0.250000000
I	0.000000000	0.000000000	0.583333015
I	0.333332987	0.666666996	0.583333015
I	0.666666971	0.333332998	0.583333015
I	0.333332982	0.333332998	0.916666985
I	0.666666955	0.000000000	0.916666985
I	0.000000020	0.666666996	0.916666985
Ir	0.666666976	0.666666996	0.083332998
Ir	0.333332982	0.333332998	0.416667019
Ir	0.666666971	0.333332998	0.750000000
Ir	0.333332966	0.000000000	0.083332998
Ir	0.666666955	0.000000000	0.416667019
Ir	0.333332987	0.666666996	0.750000000
A	0.000000016	0.333332998	0.083332998
A	0.000000020	0.666666996	0.416667019
A	-0.000000000	-0.000000000	0.750000000
O	0.333332982	0.333332998	0.000000000
O	0.666666955	0.000000000	0.000000000
O	0.000000020	0.666666996	0.000000000
O	0.000000000	0.000000000	0.166667002
O	0.333332987	0.666666996	0.166667002
O	0.666666971	0.333332998	0.166667002
O	-0.000000000	-0.000000000	0.333332981
O	0.333332987	0.666666996	0.333332981
O	0.666666971	0.333332998	0.333332981
O	0.333332966	0.000000000	0.500000000
O	0.666666976	0.666666996	0.500000000
O	0.000000016	0.333332998	0.500000000
O	0.333332966	-0.000000000	0.666666985
O	0.666666976	0.666666996	0.666666985
O	0.000000016	0.333332998	0.666666985
O	0.333332982	0.333332998	0.833333015
O	0.666666955	0.000000000	0.833333015
O	0.000000020	0.666666996	0.833333015
$\mathbf{v}_1 = (6.0621781349, 0.0000000000, 0.0000000000)$			
$\mathbf{v}_2 = (-3.0310890675, 5.2500002671, 0.0000000000)$			
$\mathbf{v}_3 = (0.0000000000, 0.0000000000, 14.0000000000)$			

Table B.2: Lattice parameters for the layer stacking P3.

Stacking T1-AB			
Atom	x	y	z
I	0.333333	0.333333	0.375000
I	0.666667	0.000000	0.375000
I	1.000000	0.666667	0.375000
I	0.000000	0.000000	0.875000
I	0.333333	0.666667	0.875000
I	0.666667	0.333333	0.875000
Ir	0.333333	1.000000	0.125000
Ir	0.666667	0.666667	0.125000
Ir	0.333333	1.000000	0.625000
Ir	0.666667	0.666667	0.625000
A	0.000000	0.333333	0.125000
A	0.000000	0.333333	0.625000
O	0.333333	0.333333	0.000000
O	0.666667	0.000000	1.000000
O	1.000000	0.666667	0.000000
O	0.000000	0.000000	0.250000
O	0.333333	0.666667	0.250000
O	0.666667	0.333333	0.250000
O	0.333333	0.333333	0.500000
O	0.666667	0.000000	0.500000
O	1.000000	0.666667	0.500000
O	0.000000	0.000000	0.750000
O	0.333333	0.666667	0.750000
O	0.666667	0.333333	0.750000
$\mathbf{v}_1 = (5.250000, 3.031089, 0.000000)$			
$\mathbf{v}_2 = (-5.250000, 3.031089, -0.000000)$			
$\mathbf{v}_3 = (-0.000000, -0.000000, 9.340000)$			

Stacking T1-AC			
Atom	x	y	z
I	0.333333	0.333333	0.375000
I	0.666667	0.000000	0.375000
I	1.000000	0.666667	0.375000
I	0.333333	1.000000	0.875000
I	0.666667	0.666667	0.875000
I	0.000000	0.333333	0.875000
Ir	0.333333	1.000000	0.125000
Ir	0.666667	0.666667	0.125000
Ir	0.333333	1.000000	0.625000
Ir	0.666667	0.666667	0.625000
A	0.000000	0.333333	0.125000
A	0.000000	0.333333	0.625000
O	0.333333	0.333333	0.000000
O	0.666667	0.000000	1.000000
O	1.000000	0.666667	0.000000
O	0.000000	0.000000	0.250000
O	0.333333	0.666667	0.250000
O	0.666667	0.333333	0.250000
O	0.333333	0.333333	0.500000
O	0.666667	0.000000	0.500000
O	1.000000	0.666667	0.500000
O	0.000000	0.000000	0.750000
O	0.333333	0.666667	0.750000
O	0.666667	0.333333	0.750000
$\mathbf{v}_1 = (5.250000, 3.031089, 0.000000)$			
$\mathbf{v}_2 = (-5.250000, 3.031089, -0.000000)$			
$\mathbf{v}_3 = (-0.000000, -0.000000, 9.340000)$			

Stacking T1-BA			
Atom	x	y	z
I	0.333333	0.333333	0.875000
I	0.666667	0.000000	0.875000
I	1.000000	0.666667	0.875000
I	0.000000	0.000000	0.375000
I	0.333333	0.666667	0.375000
I	0.666667	0.333333	0.375000
Ir	0.333333	1.000000	0.125000
Ir	0.666667	0.666667	0.125000
Ir	0.333333	1.000000	0.625000
Ir	0.666667	0.666667	0.625000
A	0.000000	0.333333	0.125000
A	0.000000	0.333333	0.625000
O	0.333333	0.333333	0.000000
O	0.666667	0.000000	1.000000
O	1.000000	0.666667	0.000000
O	0.000000	0.000000	0.250000
O	0.333333	0.666667	0.250000
O	0.666667	0.333333	0.250000
O	0.333333	0.333333	0.500000
O	0.666667	0.000000	0.500000
O	1.000000	0.666667	0.500000
O	0.000000	0.000000	0.750000
O	0.333333	0.666667	0.750000
O	0.666667	0.333333	0.750000
$\mathbf{v}_1 = (5.250000, 3.031089, 0.000000)$			
$\mathbf{v}_2 = (-5.250000, 3.031089, -0.000000)$			
$\mathbf{v}_3 = (-0.000000, -0.000000, 9.340000)$			

Stacking T1-BC			
Atom	x	y	z
I	0.000000	0.000000	0.375000
I	0.333333	0.666667	0.375000
I	0.666667	0.333333	0.375000
I	0.333333	1.000000	0.875000
I	0.666667	0.666667	0.875000
I	0.000000	0.333333	0.875000
Ir	0.333333	1.000000	0.125000
Ir	0.666667	0.666667	0.125000
Ir	0.333333	1.000000	0.625000
Ir	0.666667	0.666667	0.625000
A	0.000000	0.333333	0.125000
A	0.000000	0.333333	0.625000
O	0.333333	0.333333	0.000000
O	0.666667	0.000000	1.000000
O	1.000000	0.666667	0.000000
O	0.000000	0.000000	0.250000
O	0.333333	0.666667	0.250000
O	0.666667	0.333333	0.250000
O	0.333333	0.333333	0.500000
O	0.666667	0.000000	0.500000
O	1.000000	0.666667	0.500000
O	0.000000	0.000000	0.750000
O	0.333333	0.666667	0.750000
O	0.666667	0.333333	0.750000
$\mathbf{v}_1 = (5.250000, 3.031089, 0.000000)$			
$\mathbf{v}_2 = (-5.250000, 3.031089, -0.000000)$			
$\mathbf{v}_3 = (-0.000000, -0.000000, 9.340000)$			

Stacking T1-CA			
Atom	x	y	z
I	0.333333	1.000000	0.375000
I	0.666667	0.666667	0.375000
I	0.000000	0.333333	0.375000
I	0.333333	0.333333	0.875000
I	0.666667	0.000000	0.875000
I	1.000000	0.666667	0.875000
Ir	0.333333	1.000000	0.125000
Ir	0.666667	0.666667	0.125000
Ir	0.333333	1.000000	0.625000
Ir	0.666667	0.666667	0.625000
A	0.000000	0.333333	0.125000
A	0.000000	0.333333	0.625000
O	0.333333	0.333333	0.000000
O	0.666667	0.000000	1.000000
O	1.000000	0.666667	0.000000
O	0.000000	0.000000	0.250000
O	0.333333	0.666667	0.250000
O	0.666667	0.333333	0.250000
O	0.333333	0.333333	0.500000
O	0.666667	0.000000	0.500000
O	1.000000	0.666667	0.500000
O	0.000000	0.000000	0.750000
O	0.333333	0.666667	0.750000
O	0.666667	0.333333	0.750000
$\mathbf{v}_1 = (5.250000, 3.031089, 0.000000)$			
$\mathbf{v}_2 = (-5.250000, 3.031089, -0.000000)$			
$\mathbf{v}_3 = (-0.000000, -0.000000, 9.340000)$			

Stacking T1-CB			
Atom	x	y	z
I	0.333333	1.000000	0.375000
I	0.666667	0.666667	0.375000
I	0.000000	0.333333	0.375000
I	0.000000	0.000000	0.875000
I	0.333333	0.666667	0.875000
I	0.666667	0.333333	0.875000
Ir	0.333333	1.000000	0.125000
Ir	0.666667	0.666667	0.125000
Ir	0.333333	1.000000	0.625000
Ir	0.666667	0.666667	0.625000
A	0.000000	0.333333	0.125000
A	0.000000	0.333333	0.625000
O	0.333333	0.333333	0.000000
O	0.666667	0.000000	1.000000
O	1.000000	0.666667	0.000000
O	0.000000	0.000000	0.250000
O	0.333333	0.666667	0.250000
O	0.666667	0.333333	0.250000
O	0.333333	0.333333	0.500000
O	0.666667	0.000000	0.500000
O	1.000000	0.666667	0.500000
O	0.000000	0.000000	0.750000
O	0.333333	0.666667	0.750000
O	0.666667	0.333333	0.750000
$\mathbf{v}_1 = (5.250000, 3.031089, 0.000000)$			
$\mathbf{v}_2 = (-5.250000, 3.031089, -0.000000)$			
$\mathbf{v}_3 = (-0.000000, -0.000000, 9.340000)$			

Table B.3: Lattice parameters for the layer stacking T1.

Stacking P2-AB			
Atom	x	y	z
I	0.333333	0.333333	0.375000
I	0.666667	0.000000	0.375000
I	1.000000	0.666667	0.375000
I	0.000000	0.000000	0.875000
I	0.333333	0.666667	0.875000
I	0.666667	0.333333	0.875000
Ir	0.333333	1.000000	0.125000
Ir	0.666667	0.666667	0.125000
Ir	0.333333	1.000000	0.625000
Ir	0.666667	0.666667	0.625000
A	0.000000	0.333333	0.125000
A	0.000000	0.333333	0.625000
O	0.333333	0.333333	0.000000
O	0.666667	0.000000	1.000000
O	1.000000	0.666667	0.000000
O	0.000000	0.000000	0.250000
O	0.333333	0.666667	0.250000
O	0.666667	0.333333	0.250000
O	0.000000	0.000000	0.500000
O	0.333333	0.666667	0.500000
O	0.666667	0.333333	0.500000
O	0.333333	0.333333	0.750000
O	0.666667	0.000000	0.750000
O	1.000000	0.666667	0.750000
$\mathbf{v}_1 = (5.250000, 3.031089, 0.000000)$			
$\mathbf{v}_2 = (-5.250000, 3.031089, -0.000000)$			
$\mathbf{v}_3 = (-0.000000, -0.000000, 9.340000)$			

Stacking P2-AC			
Atom	x	y	z
I	0.333333	0.333333	0.375000
I	0.666667	0.000000	0.375000
I	1.000000	0.666667	0.375000
I	0.333333	1.000000	0.875000
I	0.666667	0.666667	0.875000
I	0.000000	0.333333	0.875000
Ir	0.333333	1.000000	0.125000
Ir	0.666667	0.666667	0.125000
Ir	0.333333	1.000000	0.625000
Ir	0.666667	0.666667	0.625000
A	0.000000	0.333333	0.125000
A	0.000000	0.333333	0.625000
O	0.333333	0.333333	0.000000
O	0.666667	0.000000	1.000000
O	1.000000	0.666667	0.000000
O	0.000000	0.000000	0.250000
O	0.333333	0.666667	0.250000
O	0.666667	0.333333	0.250000
O	0.000000	0.000000	0.500000
O	0.333333	0.666667	0.500000
O	0.666667	0.333333	0.500000
O	0.333333	0.333333	0.750000
O	0.666667	0.000000	0.750000
O	1.000000	0.666667	0.750000
$\mathbf{v}_1 = (5.250000, 3.031089, 0.000000)$			
$\mathbf{v}_2 = (-5.250000, 3.031089, -0.000000)$			
$\mathbf{v}_3 = (-0.000000, -0.000000, 9.340000)$			

Stacking P2-BA			
Atom	x	y	z
I	0.333333	0.333333	0.875000
I	0.666667	0.000000	0.875000
I	1.000000	0.666667	0.875000
I	0.000000	0.000000	0.375000
I	0.333333	0.666667	0.375000
I	0.666667	0.333333	0.375000
Ir	0.333333	1.000000	0.125000
Ir	0.666667	0.666667	0.125000
Ir	0.333333	1.000000	0.625000
Ir	0.666667	0.666667	0.625000
A	0.000000	0.333333	0.125000
A	0.000000	0.333333	0.625000
O	0.333333	0.333333	0.000000
O	0.666667	0.000000	1.000000
O	1.000000	0.666667	0.000000
O	0.000000	0.000000	0.250000
O	0.333333	0.666667	0.250000
O	0.666667	0.333333	0.250000
O	0.000000	0.000000	0.500000
O	0.333333	0.666667	0.500000
O	0.666667	0.333333	0.500000
O	0.333333	0.333333	0.750000
O	0.666667	0.000000	0.750000
O	1.000000	0.666667	0.750000
$\mathbf{v}_1 = (5.250000, 3.031089, 0.000000)$			
$\mathbf{v}_2 = (-5.250000, 3.031089, -0.000000)$			
$\mathbf{v}_3 = (-0.000000, -0.000000, 9.340000)$			

Stacking P2-BC			
Atom	x	y	z
I	0.000000	0.000000	0.375000
I	0.333333	0.666667	0.375000
I	0.666667	0.333333	0.375000
I	0.333333	1.000000	0.875000
I	0.666667	0.666667	0.875000
I	0.000000	0.333333	0.875000
Ir	0.333333	1.000000	0.125000
Ir	0.666667	0.666667	0.125000
Ir	0.333333	1.000000	0.625000
Ir	0.666667	0.666667	0.625000
A	0.000000	0.333333	0.125000
A	0.000000	0.333333	0.625000
O	0.333333	0.333333	0.000000
O	0.666667	0.000000	1.000000
O	1.000000	0.666667	0.000000
O	0.000000	0.000000	0.250000
O	0.333333	0.666667	0.250000
O	0.666667	0.333333	0.250000
O	0.000000	0.000000	0.500000
O	0.333333	0.666667	0.500000
O	0.666667	0.333333	0.500000
O	0.333333	0.333333	0.750000
O	0.666667	0.000000	0.750000
O	1.000000	0.666667	0.750000
$\mathbf{v}_1 = (5.250000, 3.031089, 0.000000)$			
$\mathbf{v}_2 = (-5.250000, 3.031089, -0.000000)$			
$\mathbf{v}_3 = (-0.000000, -0.000000, 9.340000)$			

Stacking P2-CA			
Atom	x	y	z
I	0.333333	1.000000	0.375000
I	0.666667	0.666667	0.375000
I	0.000000	0.333333	0.375000
I	0.333333	0.333333	0.875000
I	0.666667	0.000000	0.875000
I	1.000000	0.666667	0.875000
Ir	0.333333	1.000000	0.125000
Ir	0.666667	0.666667	0.125000
Ir	0.333333	1.000000	0.625000
Ir	0.666667	0.666667	0.625000
A	0.000000	0.333333	0.125000
A	0.000000	0.333333	0.625000
O	0.333333	0.333333	0.000000
O	0.666667	0.000000	1.000000
O	1.000000	0.666667	0.000000
O	0.000000	0.000000	0.250000
O	0.333333	0.666667	0.250000
O	0.666667	0.333333	0.250000
O	0.000000	0.000000	0.500000
O	0.333333	0.666667	0.500000
O	0.666667	0.333333	0.500000
O	0.333333	0.333333	0.750000
O	0.666667	0.000000	0.750000
O	1.000000	0.666667	0.750000
$\mathbf{v}_1 = (5.250000, 3.031089, 0.000000)$			
$\mathbf{v}_2 = (-5.250000, 3.031089, -0.000000)$			
$\mathbf{v}_3 = (-0.000000, -0.000000, 9.340000)$			

Stacking P2-CB			
Atom	x	y	z
I	0.333333	1.000000	0.375000
I	0.666667	0.666667	0.375000
I	0.000000	0.333333	0.375000
I	0.000000	0.000000	0.875000
I	0.333333	0.666667	0.875000
I	0.666667	0.333333	0.875000
Ir	0.333333	1.000000	0.125000
Ir	0.666667	0.666667	0.125000
Ir	0.333333	1.000000	0.625000
Ir	0.666667	0.666667	0.625000
A	0.000000	0.333333	0.125000
A	0.000000	0.333333	0.625000
O	0.333333	0.333333	0.000000
O	0.666667	0.000000	1.000000
O	1.000000	0.666667	0.000000
O	0.000000	0.000000	0.250000
O	0.333333	0.666667	0.250000
O	0.666667	0.333333	0.250000
O	0.000000	0.000000	0.500000
O	0.333333	0.666667	0.500000
O	0.666667	0.333333	0.500000
O	0.333333	0.333333	0.750000
O	0.666667	0.000000	0.750000
O	1.000000	0.666667	0.750000
$\mathbf{v}_1 = (5.250000, 3.031089, 0.000000)$			
$\mathbf{v}_2 = (-5.250000, 3.031089, -0.000000)$			
$\mathbf{v}_3 = (-0.000000, -0.000000, 9.340000)$			

Table B.4: Lattice parameters for the layer stacking P2.

Bibliography

[1] Leon Balents. Spin liquids in frustrated magnets. *Nature*, 464(7286): 199, 2010.

[2] MR Norman. Colloquium: Herbertsmithite and the search for the quantum spin liquid. *Reviews of Modern Physics*, 88(4):041002, 2016.

[3] Maria Hermanns, Itamar Kimchi, and Johannes Knolle. Physics of the Kitaev model: fractionalization, dynamical correlations, and material connections. *Annual Review of Condensed Matter Physics*, (0), 2017.

[4] Alexei Kitaev. Anyons in an exactly solved model and beyond. *Annals of Physics*, 321(1):2–111, 2006.

[5] Johannes Reuther, Ronny Thomale, and Stephan Rachel. Spiral order in the honeycomb iridate Li_2IrO_3. *Physical Review B*, 90(10):100405, 2014.

[6] Jiří Chaloupka, George Jackeli, and Giniyat Khaliullin. Zigzag magnetic order in the iridium oxide Na_2IrO_3. *Physical Review Letters*, 110(9): 097204, 2013.

[7] Gang Cao and Pedro Schlottmann. The challenge of spin-orbit-tuned ground states in iridates: A key issues review. *Reports on Progress in Physics*, 2018.

[8] Abhijit Biswas, Ki-Seok Kim, and Yoon Hee Jeong. Metal-insulator transitions and non-fermi liquid behaviors in $5d$ perovskite iridates. *arXiv preprint arXiv:1508.04929*, 2015.

[9] S.K. Choi, R. Coldea, A.N. Kolmogorov, T. Lancaster, I.I. Mazin, S.J. Blundell, P.G. Radaelli, Yogesh Singh, P. Gegenwart, K.R. Choi, et al. Spin waves and revised crystal structure of honeycomb iridate Na_2IrO_3. *Physical Review Letters*, 108(12):127204, 2012.

[10] Sebastian Bette, Tomohiro Takayama, Kentaro Kitagawa, Riku Takano, Hidenori Takagi, and Robert E. Dinnebier. Solution of the heavily stacking faulted crystal structure of the honeycomb iridate $H_3LiIr_2O_6$. *Dalton Transactions*, 46(44):15216–15227, 2017.

[11] Kavita Mehlawat, A. Thamizhavel, and Yogesh Singh. Heat capacity evidence for proximity to the Kitaev quantum spin liquid in A_2IrO_3 (A= Na, Li). *Physical Review B*, 95(14):144406, 2017.

[12] K. Kitagawa, T. Takayama, Y. Matsumoto, A. Kato, R. Takano, Y. Kishimoto, S. Bette, R. Dinnebier, G. Jackeli, and H. Takagi. A spin-orbital-entangled quantum liquid on a honeycomb lattice. *Nature*, 554(7692):341, 2018.

[13] Paolo Giannozzi, Stefano Baroni, Nicola Bonini, Matteo Calandra, Roberto Car, Carlo Cavazzoni, Davide Ceresoli, Guido L. Chiarotti, Matteo Cococcioni, Ismaila Dabo, et al. QUANTUM ESPRESSO: a modular and open-source software project for quantum simulations of materials. *Journal of physics: Condensed matter*, 21(39):395502, 2009.

[14] Georg Kresse and Jürgen Hafner. Ab initio molecular dynamics for liquid metals. *Physical Review B*, 47(1):558, 1993.

[15] Georg Kresse and Jürgen Hafner. Ab initio molecular-dynamics simulation of the liquid-metal–amorphous-semiconductor transition in germanium. *Physical Review B*, 49(20):14251, 1994.

[16] Georg Kresse and Jürgen Furthmüller. Efficiency of ab-initio total energy calculations for metals and semiconductors using a plane-wave basis set. *Computational materials science*, 6(1):15–50, 1996.

[17] Georg Kresse and Jürgen Furthmüller. Efficient iterative schemes for ab initio total-energy calculations using a plane-wave basis set. *Physical review B*, 54(16):11169, 1996.

[18] Matteo Cococcioni and Stefano De Gironcoli. Linear response approach to the calculation of the effective interaction parameters in the LDA+U method. *Physical Review B*, 71(3):035105, 2005.

[19] Claude Delmas, Claude Fouassier, and Paul Hagenmuller. Structural classification and properties of the layered oxides. *Physica B+ C*, 99 (1-4):81–85, 1980.

[20] Koichi Momma and Fujio Izumi. VESTA: a three-dimensional visualization system for electronic and structural analysis. *Journal of Applied Crystallography*, 41(3):653–658, 2008.

[21] S Curtarolo, GLW Hart, W Setyawan, M Mehl, M Jahnatek, RV Chepulskii, O Levy, and D Morgan. AFLOW: software for high-throughput calculation of material properties, 2009.